

## RESEARCH ARTICLE

10.1002/2016JE005247

## Key Points:

- Comprehensive geologic investigation and mapping of Mons Rümker were conducted
- Multiple stages of volcanic activities happened on Mons Rümker from Imbrian to Eratosthenian
- Two candidate landing sites were proposed for China's Chang'E-5 sample return mission

## Supporting Information:

- Supporting Information S1

## Correspondence to:

L. Xiao,  
longxiao@cug.edu.cn

## Citation:

Zhao, J., L. Xiao, L. Qiao, T. D. Glotch, and Q. Huang (2017), The Mons Rümker volcanic complex of the Moon: A candidate landing site for the Chang'E-5 mission, *J. Geophys. Res. Planets*, 122, 1419–1442, doi:10.1002/2016JE005247.

Received 18 DEC 2016

Accepted 14 JUN 2017

Accepted article online 27 JUN 2017

Published online 12 JUL 2017

## The Mons Rümker volcanic complex of the Moon: A candidate landing site for the Chang'E-5 mission

Jiannan Zhao<sup>1,3</sup> , Long Xiao<sup>1,2</sup> , Le Qiao<sup>1</sup>, Timothy D. Glotch<sup>3</sup> , and Qian Huang<sup>1</sup> 

<sup>1</sup>State Key Laboratory of Geological Process and Mineral Resources, Planetary Science Institute, School of Earth Sciences, China University of Geosciences, Wuhan, China, <sup>2</sup>Space Science Institute, Lunar and Planetary Science Laboratory, Macau University of Science and Technology, Macau, China, <sup>3</sup>Department of Geosciences, State University of New York at Stony Brook, Stony Brook, New York, USA

**Abstract** Mons Rümker is a large volcanic complex in Oceanus Procellarum on the Moon and is a candidate landing site for China's Chang'E-5 sample return mission. We conducted a comprehensive study of the topography, geomorphology, composition, and stratigraphy of the Mons Rümker region with multisource remote sensing data in order to better understand the geology of the region and provide further support for the Chang'E-5 mission. The results show that the Rümker plateau stands 200–1300 m above the surrounding mare surface and 75% of the plateau has a slope of less than 3° at a baseline length of 30 m. Domes are the most prominent volcanic landforms in Mons Rümker and a total of 22 domes were identified and divided into two types that may represent different stages of volcanic activity. Spectral analyses indicated that Mons Rümker is covered by low-Ti basalt and the dominant mafic mineral is high-calcium pyroxene, though signs of mixing of highland materials and basalt have been found. Mons Rümker has three main basalt units, and their absolute model ages are 3.71 Ga, 3.58 Ga, and 3.51 Ga, respectively. Steep-sided domes could be the youngest volcanic features on the plateau with indications that they were active until the Eratosthenian. A new geologic map of the study region was produced and used to interpret and discuss the geologic evolution of the region. Finally, we propose two candidate landing sites for the Chang'E-5 mission.

### 1. Introduction

The Chang'E-5 mission is the third stage of the Chinese Lunar Exploration Program. The spacecraft is scheduled to launch in 2017 and will bring back up to 2 kg of lunar surface regolith and drill core samples [Zou and Li, 2017]. The northern Oceanus Procellarum has been selected as the landing region, where Mons Rümker is an outstanding volcanic complex and is a priority candidate landing site for Chang'E-5 (Figure 1).

The Mons Rümker region is centered at 301.9°E, 40.7°N and comprises a plateau with an area of ~4000 km<sup>2</sup>. A great many volcanic features such as domes, sinuous rilles, and lava flows are concentrated in this region [Scott and Eggleton, 1973; Smith, 1974]. There are two main geologic units according to the 1:1 million scale geologic map produced by Scott and Eggleton [1973]: the lineated terrain (Figure 2) in the north and the plateau-forming materials occupying the main part of Mons Rümker. The lineated terrain is considered to be part of the Fra Mauro Formation, which is the ejecta blanket from the giant impact that formed the Imbrium basin. Smith [1974] studied the geomorphology of Mons Rümker and made a detailed geologic map of the region. Smith [1974] identified over 30 volcanic domes and classified them into three types according to their shape, diameter, and stratigraphic relationship. However, this work is mainly based on Lunar Orbiter imagery data, and the dome identification could be improved upon with more recent topographic data. Campbell *et al.* [2009] analyzed the surface properties of Mons Rümker with Earth-based radar data and found that it was likely to be covered by rock-poor, fine-grained pyroclastic materials. Wöhler *et al.* [2007a] analyzed the morphometry and rheology of several domes on the Rümker plateau. They suggested that the domes were formed at low effusion rates and the Rümker plateau was fed by a dike with its magma source located at the bottom of or below the lunar crust. Spudis *et al.* [2013] proposed that Mons Rümker is a large shield volcano. Farrand *et al.* [2015] further analyzed possible pyroclastic mantles using SELENE Multiband Imager (MI) and Chandrayaan Moon Mineralogy Mapper (M<sup>3</sup>) data, but they did not present strong evidence for the existence of pyroclastic materials.

However, compared with other large volcanic complexes in Oceanus Procellarum (e.g., Marius Hills [Weitz and Head, 1999; Heather *et al.*, 2003; Besse *et al.*, 2011; Huang *et al.*, 2011; Lawrence *et al.*, 2013] and Aristarchus

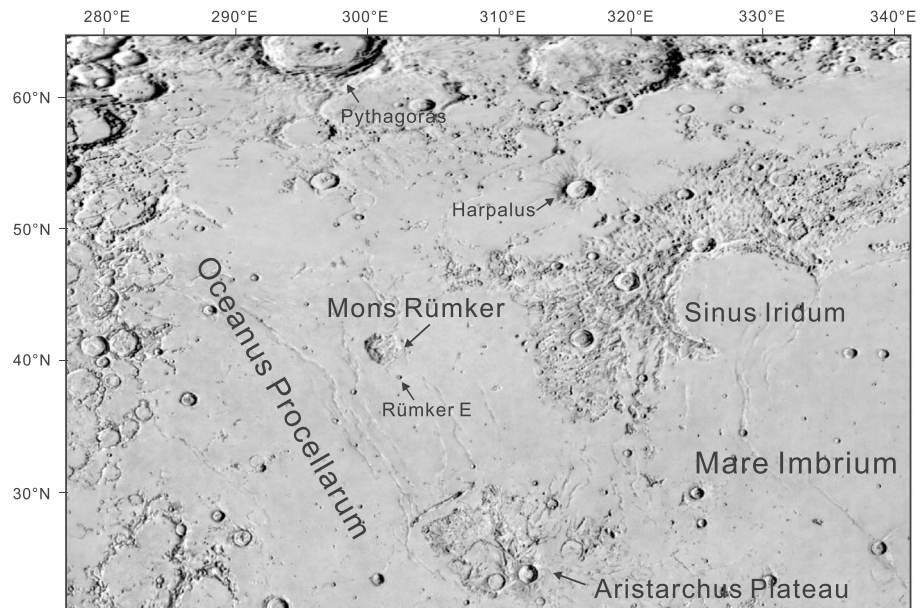


**Figure 1.** Location of Mons Rümker. The background is U.S. Geological Survey lunar airbrushed shaded relief map (simple cylindrical projection; [https://webgis.wr.usgs.gov/pigwad/down/moon\\_airbrushed\\_shadedrelief\\_warp.htm](https://webgis.wr.usgs.gov/pigwad/down/moon_airbrushed_shadedrelief_warp.htm)).

plateau [McEwen *et al.*, 1994; Le Mouélic *et al.*, 2000; Campbell *et al.*, 2008; Chevrel *et al.*, 2009; Hagerty *et al.*, 2009; Mustard *et al.*, 2011; Zhang *et al.*, 2014]), Mons Rümker is still poorly understood. The formation mechanism of some geologic features (e.g., domes) in this region is poorly constrained, and the geologic evolutionary history of Mons Rümker is still unclear. In addition, there has been no detailed and systematic study of this area, which is required for landing site selection for a sample return mission. Therefore, in this work, we present a comprehensive study of the topography, geomorphologic features, composition, and stratigraphy of the Mons Rümker region utilizing the latest high-quality remote sensing data, so that we can get a better understanding on the geology of the region and provide supports for the Chang'E-5 mission.

## 2. Topography and Geomorphology

### 2.1. Regional Topography

A global digital terrain model (DTM) derived from stereo pair images from the terrain camera (TC) on board SELENE [Haruyama *et al.*, 2008] was used to analyze the topography of the study region. The spatial resolution of the data set is  $\sim 10$  m/pixel [Haruyama *et al.*, 2012], which is well suited for morphologic measurements of small features such as craters and domes. We also obtained the surface slope at a baseline length of 30 m by calculating the maximum rate of elevation change in TC DTM from the central pixel to its neighboring eight pixels in a  $3 \times 3$  analyzing window [Burrough and McDonnell, 1998].

Mons Rümker is approximately circular in shape and stands 200–1300 m above the surrounding mare surface (Figures 3a and 3c). A scarp separates the Rümker plateau from the surrounding mare plain. The central and southern parts of Mons Rümker are higher with the maximum elevation reached at the summit of a dome (“H” in Figure 3a), which is about  $-1280$  m. The lowest point occurs in the bottom of a crater in the northern lineated region (“L” in Figure 3a) with an elevation of  $-2777$  m. The slope map derived from the TC DTM shows that 75% of Mons Rümker has slopes  $< 3^\circ$ . Marginal scarps of the Rümker plateau have steeper slopes ( $5$ – $9^\circ$ ). The steepest parts are the inner walls of some craters, which can be more than  $15^\circ$  (Figure 3b).

### 2.2. Geomorphology

Identification and analysis of different geomorphologic features were mainly based on images obtained from TC and the narrow-angle camera (NAC) on board the Lunar Reconnaissance Orbiter (LRO). TC images have a spatial resolution of  $\sim 10$  m/pixel [Haruyama *et al.*, 2008], which can be used in the analysis of regional geomorphology as well as local features. In addition, these images have different illumination conditions

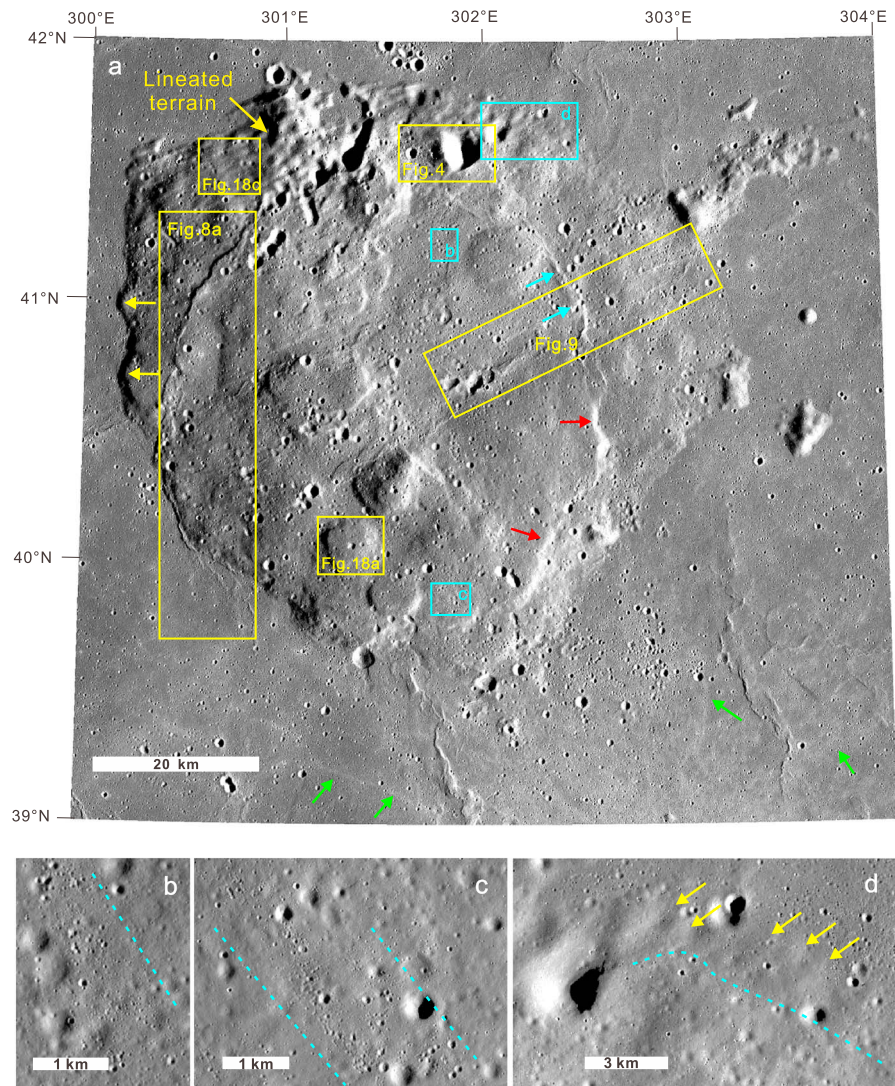


**Figure 2.** (a) SELENE terrain camera morning map of Mons Rümker (image ID: TCO\_MAPm04\_N42E300N39E303SC and TCO\_MAPm04\_N42E303N39E306SC). The central coordinates of the image are 302.0°E, 40.5°N. Yellow boxes indicate the location of other figures in this paper. Blue boxes indicate the locations of Figures 2b–2d. Yellow arrows indicate the marginal scarp of the Rümker plateau. Red arrows indicate the east scarp. Blue arrows indicate the wrinkle ridge connected to a scarp. Green arrows indicate the ejecta rays of Rümker E crater. All maps of the Mons Rümker region in this study are presented in Lambert conformal conic projection with the standard parallel at 40.5°N and the central meridian at 302.0°E unless otherwise indicated. (b) Secondary crater clusters in the northeast of Mons Rümker. The blue dashed line denotes the trending direction of the crater clusters. (c) Secondary crater clusters in the southeast of Mons Rümker. Blue dashed lines denote the trending direction of the crater clusters. (d) Superposition of younger lava unit on the linear depressions. Their contact is indicated by a blue dashed line. Yellow arrows indicate the linear depressions.

(referred to as “morning”, “evening,” and “ortho”), which can provide distinct views of geomorphologic features. In this study, TC morning images (incidence angle: ~70°) of the Mons Rümker region were used to perform crater counting in order to acquire the absolute model ages of the geologic units. NAC images have relatively high spatial resolution (~0.5 m/pixel) [Robinson *et al.*, 2010] and were used in the detailed study of small-scale geologic features.

### 2.2.1. Impact Craters

Impact craters in the Mons Rümker region are mostly bowl shaped simple craters. They are usually smaller than 2 km in diameter. A great many heavily degraded craters can be observed, indicating an old surface age of the region. There are also many irregular craters and clustered craters (Figures 2b and 2c), which are probably secondary craters. Scott and Eggleton [1973] mapped the distribution of these craters and

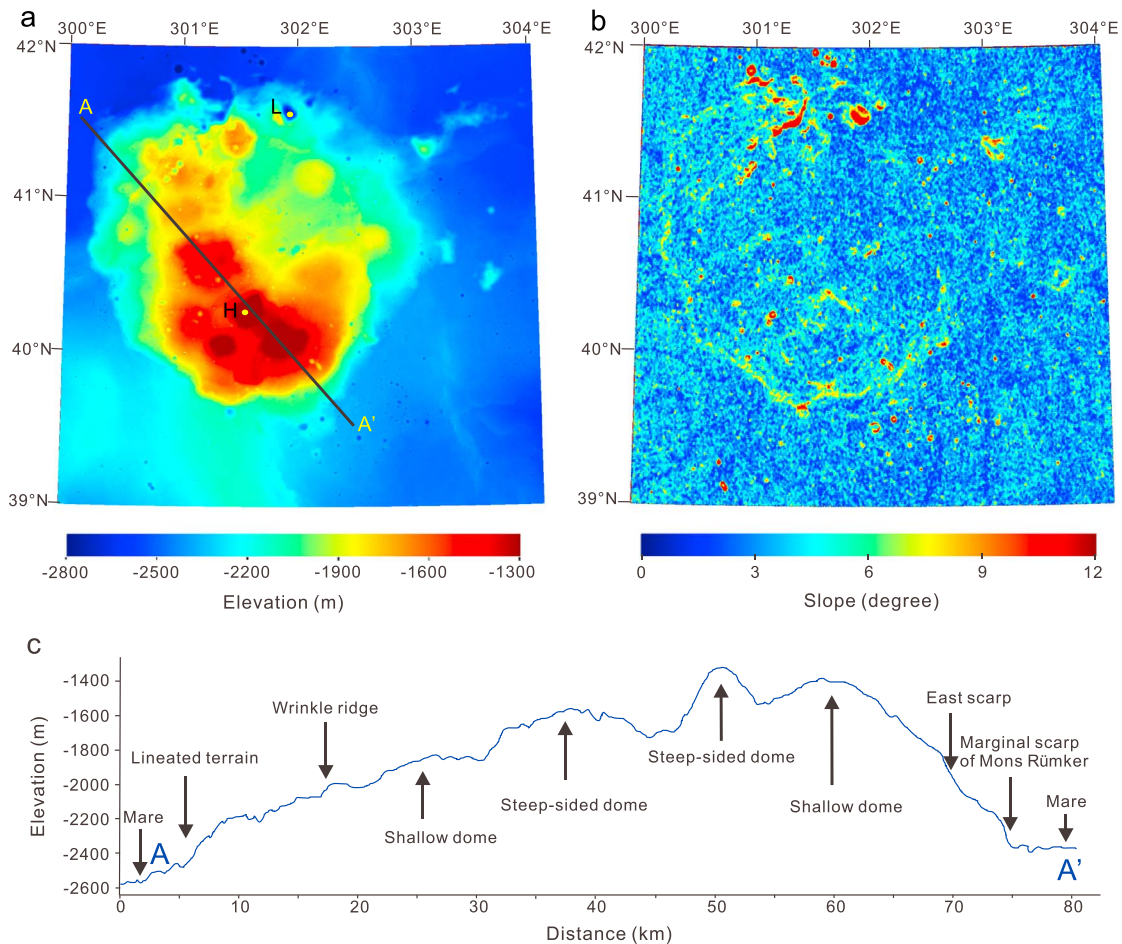


**Figure 3.** (a) Topographic map derived from TC DTM (data ID: DTM\_MAP\_02\_N42E300N39E303SC and DTM\_MAP\_02\_N42E303N39E306SC). Point H denotes the highest point and L denotes the lowest point on the Rümker plateau. The profile AA' is shown in Figure 3c. (b) Slope map of Mons Rümker. (c) Elevation profile and typical landforms along AA' in Figure 3a.

found that most of them were formed by ejecta from Copernican craters such as Aristarchus, Copernicus, Harpalus, and Pythagoras (Figure 1). For example, some NNW trending crater clusters in the northeastern Rümker plateau (Figure 2b) spread along the rays of the Pythagoras crater and thus could be secondary craters formed by Pythagoras impact. In addition, we found that the Rümker E crater is also a main source of secondary craters on the Rümker plateau. The Rümker E crater is 6.7 km in diameter and located ~25 km southeast to the Rümker plateau (Figure 1). It has several crater rays that are up to 80 km long. These crater rays have high albedo on the TC morning map (Figure 2a) and show bright yellow on the Moon Mineralogy Mapper composite map (Figure 12a; see section 3.2). Some crater clusters (Figure 2c) on southeastern Rümker plateau spread along the direction of these rays and could be also formed by ejecta of Rümker E crater.

The largest crater (central coordinates: 301.92°E, 41.59°N; Figure 4) on the Rümker plateau is located in the north of the region. It has an irregular circular shape and a diameter of ~4.3 km. The elevation of its southwest rim is about -1900 m, which is ~300 m higher than the north and east rim (Figure 4). The crater was interpreted as a collapsed volcanic pit by *Spudis et al.* [2013]. However, the crater does not resemble typical collapse pits which are usually rimless [Wyrick et al., 2004] and may not be a caldera as calderas tend to be shallow and have relatively flat floors [Wood, 1984; Burns and Campbell, 1985], whereas the crater in Figure 4 has a V-shaped profile and its floor is several hundred meters below the surface of the surrounding terrain (Figure 4b). In addition, we found no other evidence such as associated lava flows or pyroclastic deposits to support this interpretation. The crater does, however, have a higher southwest rim, and a cluster of small subdued craters located beyond the southwest rim, which could be formed by the

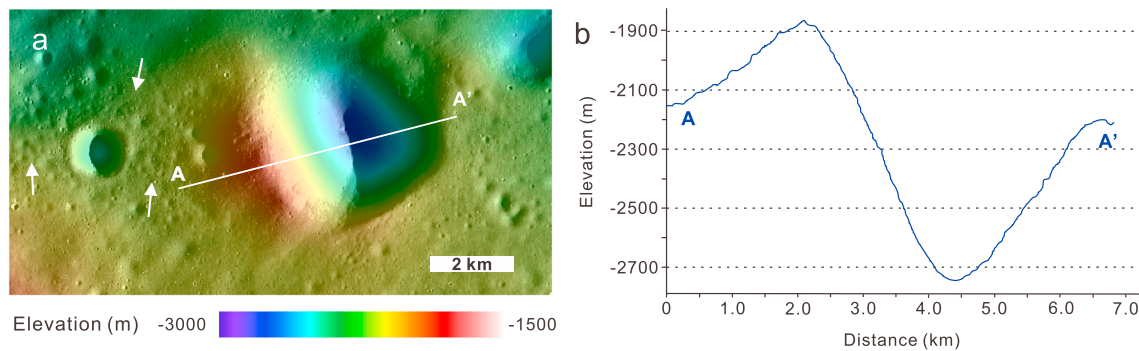


**Figure 4.** The largest crater in the Mons Rümker region. (a) TC morning map (data ID: TCO\_MAPm04\_N42E300N39E303SC) of the crater overlaid by TC DTM (data ID: DTM\_MAP\_02\_N42E300N39E303SC; central coordinates: 301.84°E, 41.57°N). White arrows point to the clustered craters. (b) Elevation profile along AA' in Figure 4a.

ejecta from this crater. This type of crater is usually formed by an oblique impact into a tilted surface [Elbeshausen *et al.*, 2012]. Therefore, a low-angle impact from the northeast onto a slope may have resulted in the formation of this crater.

### 2.2.2. Domes

Domes are the most prominent volcanic landforms on the Rümker plateau. More than 30 domes were identified by Smith [1974] using Lunar Orbiter imagery data. We checked these domes with the TC image and DTM and found some of them have no obvious topographic uplift which is the most important criterion to confirm a dome. In addition, some topographic rises controlled by local structures may be mistakenly identified as domes. We ruled out these domes and also identified some new domes in the study area. For example, Figure 5a is the Lunar Orbiter mosaic of a dome identified by Smith [1974]. It seems that this dome has a conic shape with a summit crater. However, utilizing high-resolution LRO NAC (Figure 5b) image and TC DTM (Figure 5c), we found that this feature could be part of a degraded crater rim and the summit crater is more likely a heavily degraded impact crater formed on a slope.

In this study, we identified a total of 22 domes in the Mons Rümker region (Figure 6 and Table 1). The domes are mostly near elliptical in shape and have relatively smooth surfaces. Their sizes vary from  $\sim 1.8 \times 2.2$  km to  $\sim 8.1 \times 13.6$  km with a median of  $3.9 \times 4.5$  km, and their heights are up to 400 m with a median of 130 m above the plateau surface. We obtained an average flank slope for each dome by averaging four measurements in different directions. These domes have average flank slopes of 1.9°–10.8°, and we divided them into two groups based on their flank slopes: steep-sided domes and shallow domes. Steep-sided domes are

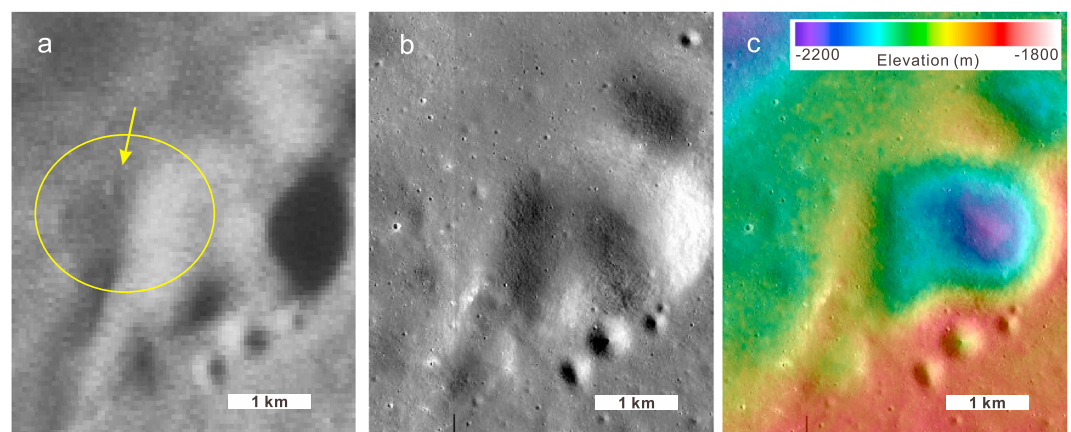


**Figure 5.** Views of a dome-like feature with different data sets. (a) Lunar Orbiter mosaic of a dome (indicated by the yellow circle, central coordinates: 300.89°E, 41.41°N) identified by Smith [1974]. The arrow points to a putative summit crater of the dome. Lunar Orbiter mosaic ID: LO\_22N292. (b) LRO NAC mosaic of the same area in Figure 5a (data ID: M1112211163LE and M1112211163RE). (c) LRO NAC mosaic of the same area in Figure 5a overlaid by TC DTM (data ID: DTM\_MAP\_02\_N42E300N39E303SC).

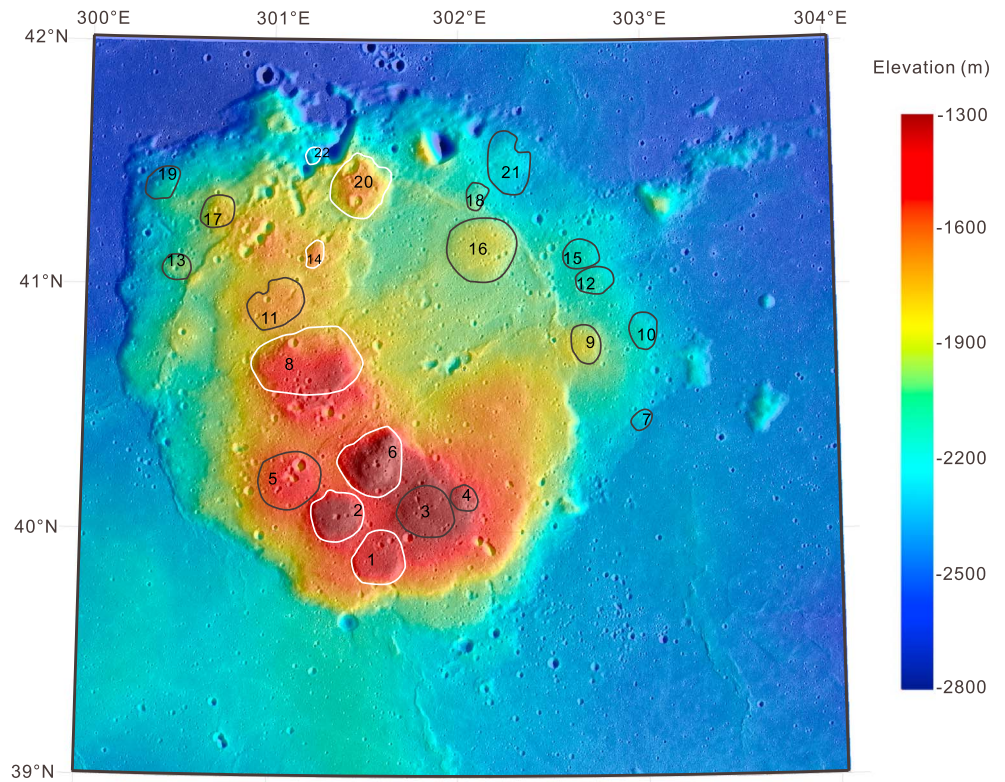


**Figure 6.** Distribution of the domes identified in this study. White lines indicate steep-sided domes. Black lines indicate shallow domes. The background is the TC morning map (data ID: TCO\_MAPm04\_N42E300N39E3035C and TCO\_MAP m04\_N42E303N39E3065C) overlaid by TC DTM (data ID: DTM\_MAP\_02\_N42E300N39E3035C and DTM\_MAP\_02\_N42E303 N39E3065C).

**Table 1.** Parameters of Domes on the Rümker Plateau

No.	Central Longitude (°E)	Central Latitude (°N)	Size (km)	Height (m)	Average Flank Slope (deg)	Type <sup>a</sup>	Associated Volcanic Feature
1	301.56	39.91	5.8 × 6.8	210	5.6	S	Pit
2	301.34	40.10	5.6 × 6.8	180	10.8	S	Pit
3	301.81	40.11	6.2 × 7.1	125	4.1	L	Pit
4	302.03	40.15	2.9 × 3.7	120	3.9	L	/
5	301.07	40.24	6.7 × 7.9	170	2.9	L	/
6	301.53	40.32	7.6 × 8.9	425	8.0	S	Pit
7	302.98	40.47	2.1 × 2.8	90	3.7	L	/
8	301.18	40.71	8.1 × 13.6	230	6.6	S	Flow feature
9	302.69	40.78	3.6 × 4.9	130	3.7	L	/
10	302.99	40.83	3.5 × 4.7	130	2.1	L	/
11	301.01	40.94	4.3 × 7.0	80	2.7	L	Rille
12	302.73	41.04	3.4 × 4.5	95	2.3	L	/
13	300.46	41.07	3.0 × 3.5	130	3.7	L	/
14	301.22	41.14	2.4 × 3.6	150	5.5	S	Pit
15	302.66	41.15	3.5 × 4.4	70	1.9	L	/
16	302.11	41.16	8.5 × 9.2	150	3.4	L	/
17	300.69	41.31	3.9 × 4.5	130	4.4	L	/
18	302.09	41.38	2.7 × 3.5	90	3.6	L	/
19	300.40	41.42	3.2 × 4.8	145	3.2	L	/
20	301.50	41.43	6.4 × 8.1	310	7.1	S	Flow feature
21	302.28	41.52	5.3 × 7.9	140	2.7	L	/
22	301.21	41.55	1.8 × 2.2	140	6.4	S	Pit

<sup>a</sup>“S” represents steep-sided dome; “L” represents shallow dome.

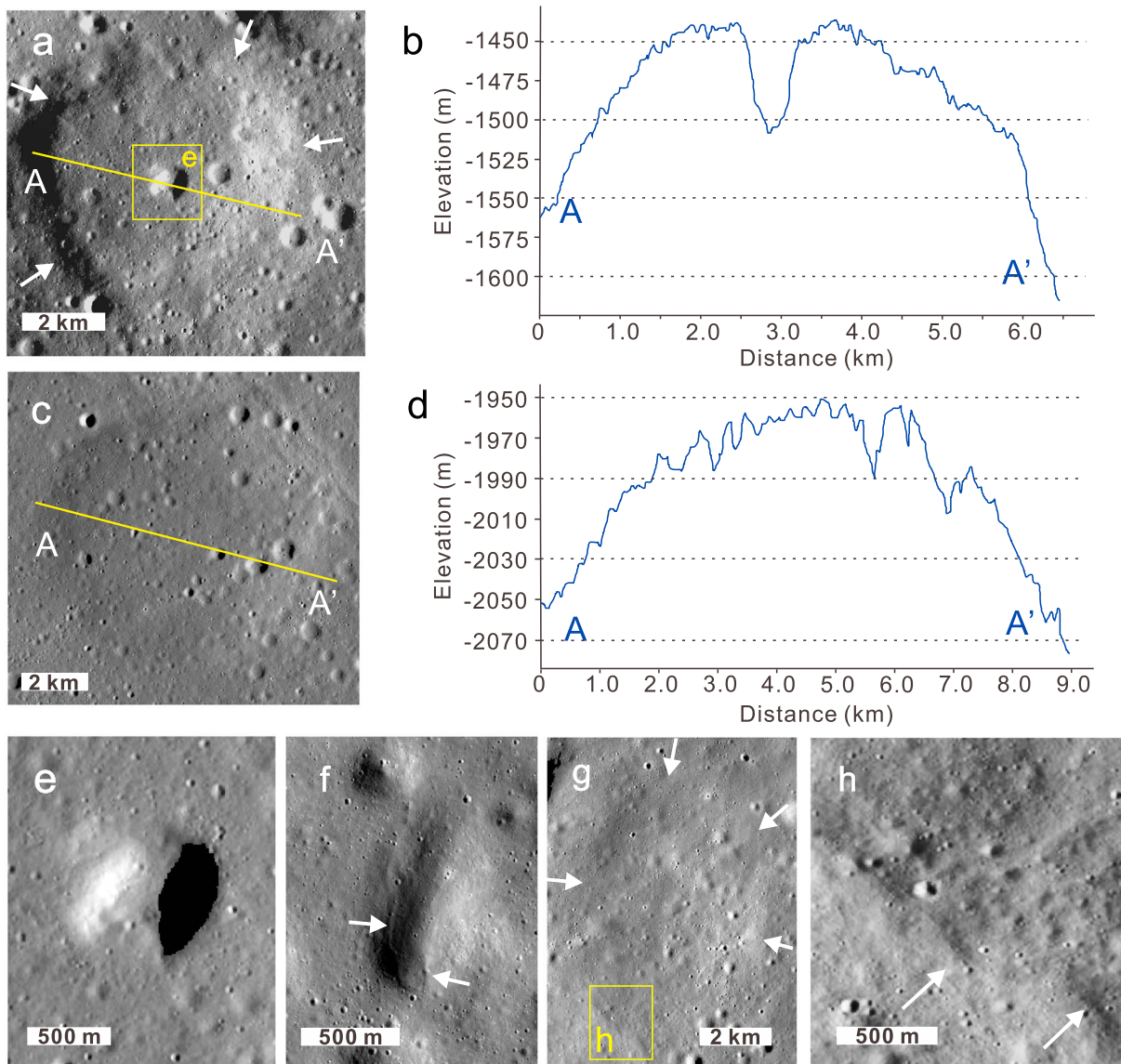


**Figure 7.** Detailed features of the domes on the Rümker plateau. IDs of the TC image and DTM used in this figure: TCO\_MAPm04\_N42E300N39E303SC and DTM\_MAP\_02\_N42E300N39E303SC. (a) TC image of a steep-sided dome (dome No. 2 in Figure 6, central coordinates: 301.34°E, 40.10°N). The suddenly elevated slope results in a distinct contact (marked as white arrows) between the dome and its surrounding terrain. The yellow line AA' is the profile line. (b) Elevation profile along AA' in Figure 7a. (c) TC image of a shallow dome (dome No. 16 in Figure 6, central coordinates: 302.11°E, 41.16°N). This dome has indistinct contact with its surrounding terrain. The yellow line AA' is the profile line. (d) Elevation profile along AA' in Figure 7c. (e) TC image of the summit pit on top of the steep-sided dome in Figure 7a. (f) A flow feature (indicated by white arrows) on the flank of dome No. 8 (central coordinates: 301.14°E, 40.58°N). LRO NAC stamp: M1142838642LE. (g) TC image of a shallow dome (dome No. 21 in Figure 6, central coordinates: 302.28°E, 41.52°N) with features of lava superposition (yellow box) on its surrounding terrain. White arrows indicate the boundary of the shallow dome. (h) Zoom of Figure 7g shows the superposition of lava on the surrounding terrain (indicated by white arrows).

characterized by relatively steep flank slopes ( $>5^\circ$ ), and their heights are usually larger than 150 m. These domes always have some associated volcanic features such as possible summit pits (Figures 7a and 7e) and flow features (Figure 7f). For example, the dome in Figure 7a is a steep-sided dome (dome No. 2). It is about 180 m in height and  $5.6 \times 6.8$  km in size. Its average flank slope is  $10.8^\circ$ . On top of the dome, an irregular rimless depression is located in the central part (Figure 7e). The rimless depression has a diameter of  $\sim 0.8$  km and a depth of 60 m. We interpret that it as a possible volcanic crater based on its irregular shape and the lack of a rim. Shallow domes have gentle flank slopes ( $<5^\circ$ ) and are all lower than 200 m. Only 2 of the 15 shallow domes have associated volcanic features (Table 1). Though most of the contacts between the shallow domes

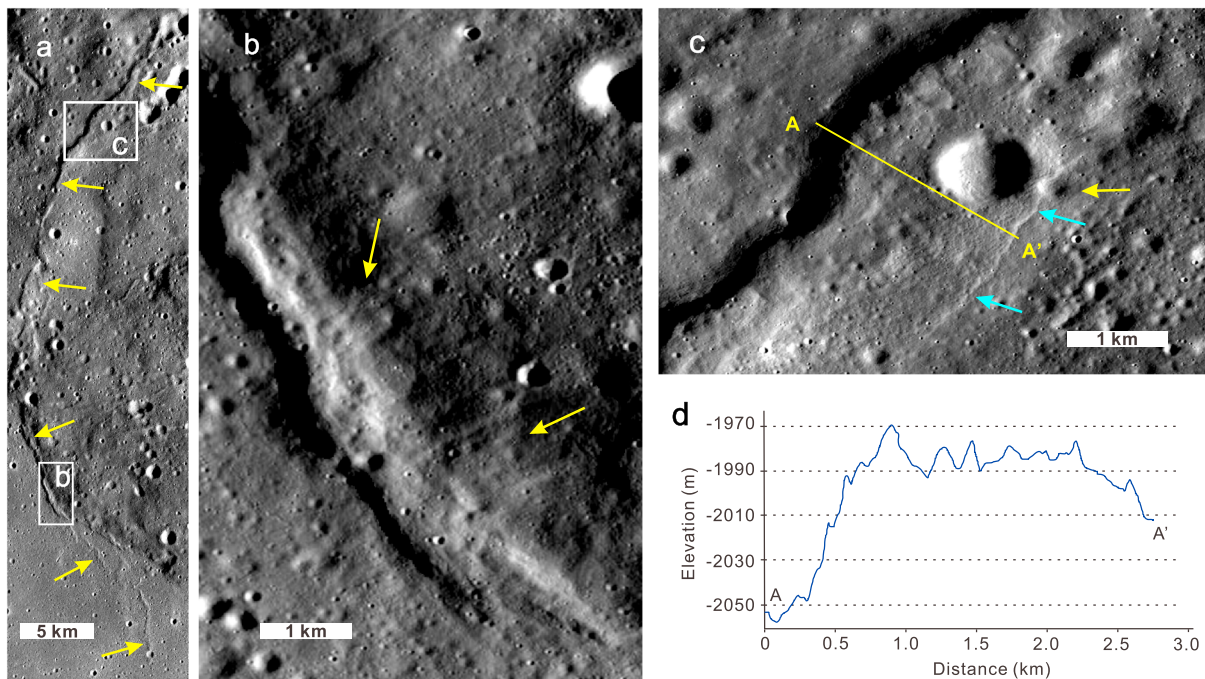


**Figure 8.** (a) TC image of a wrinkle ridge in the Mons Rümker region (central coordinates: 300.7°E, 40.5°N; TC image: TCO\_MAPm04\_N42E300N39E303SC). Yellow arrows point to the wrinkle ridge. (b) The superposition relationship (indicated by yellow arrows) between the wrinkle ridge and the scarp. (c) A lobate scarp (indicated by blue arrows) formed along the wrinkle ridge. The yellow arrow points to a crater superposing on the scarp. The elevation profile along AA' is shown in Figure 8d. (d) Elevation profile along AA' (TC DTM: DTM\_MAP\_02\_N42E300N39E303SC).

and their surrounding regions are not distinct due to the gentle flank slopes and similar surface composition, features of lava accumulation and superposition on surrounding terrains have been recognized on 14 of the 15 shallow domes (e.g., Figures 7g and 7h). Figure 7c shows the largest shallow dome (dome No. 16) on the Rümker plateau. Its size is  $8.5 \times 9.2$  km with a height of  $\sim 150$  m. The flank slope changes gradually, and the boundary between the dome and the plateau surface is not clear. Besides, it is the only shallow dome where we did not find lava overlay surrounding terrains.

### 2.2.3. Scarps and Wrinkle Ridges

Scarps develop along the rims of some steep-sided domes, the southwest margin of Mons Rümker, and in the east of the southern high-elevation area of the plateau (hereafter referred to as east scarp; indicated by red arrows in Figure 2). The slope of the marginal scarp around Mons Rümker varies from  $6^\circ$  to  $15^\circ$ , and the elevation difference is up to 400 m (Figure 3). The east scarp trends north-south and extends  $\sim 35$  km. Its northern part connects to a 23 km long wrinkle ridge (indicated by blue arrows in Figure 2) that is  $\sim 35$  m in height and 0.6–1.8 km in width. Another wrinkle ridge on the Rümker plateau is located in the west (Figure 8a). This wrinkle ridge is 60 km long and extends from the mare surface outside Mons Rümker to a large irregular crater in the north. It is 0.5–2.5 km in width and has an asymmetric traverse profile (Figure 8d) in which the elevation difference of the west side is usually much larger than the east side. This could have resulted from the existence of a previously existing scarp as the wrinkle ridge developed along and superposed on part of a scarp (Figure 8b). In addition, a small lobate scarp that is  $\sim 20$  m in height has been observed along the east side of the wrinkle ridge. Unlike most of the lunar lobate scarps which are relatively young landforms [Watters *et al.*, 2010], this lobate scarp may be old in age as it is superposed by some craters whereas no craters are observed destroyed by the scarp (Figure 8c).

### 2.2.4. Linear Depressions

Two types of linear depressions were identified in the Mons Rümker region. The first type is distributed in the northwestern part of the region (lineated terrain, Figure 2). These depressions trend east-northeast and are nearly parallel to each other. They are generally 0.5–1 km wide and several meters deep. The eastern part of the lineated terrain is buried by plateau-forming unit (Figure 2d), indicating an older age of the lineated terrain. Scott and Eggleton [1973] proposed that these linear depressions are formed by ejecta from the

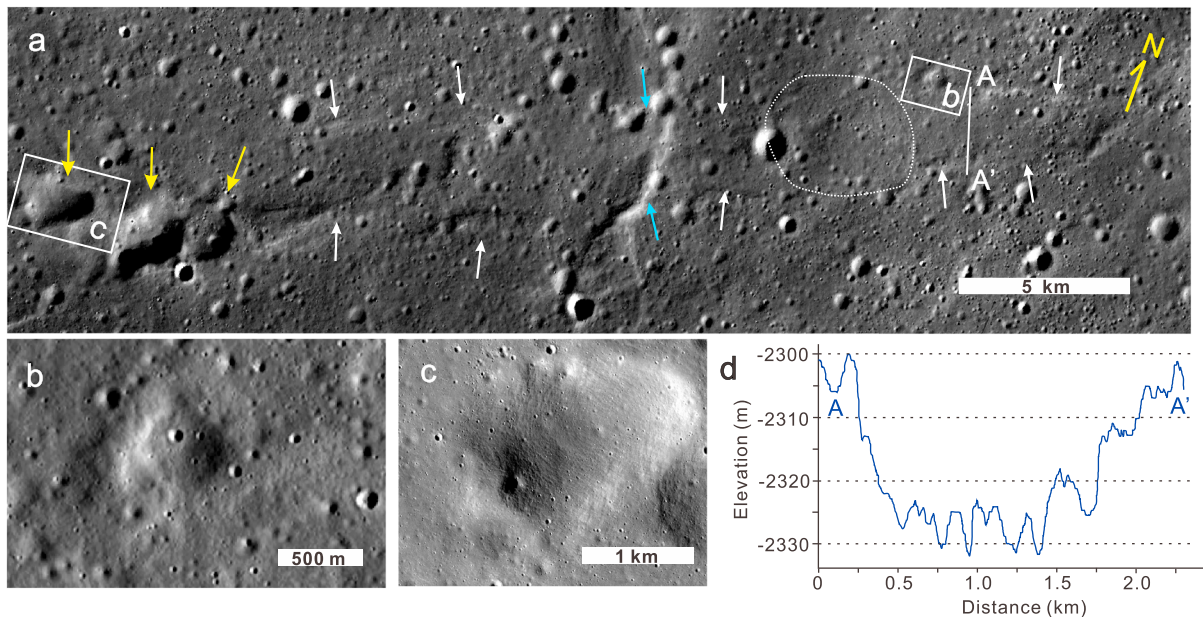


**Figure 9.** (a) The linear depression in the eastern part of Mons Rümker (central coordinates: 302.4°E, 40.9°N; TC image: TCO\_MAPm04\_N42E300N39E303SC and TCO\_MAPm04\_N42E303N39E306SC). White arrows point to the rim of the depression. Blue arrows indicate where the depression intersects the rim of the ring structure. Yellow arrows point to the rimless depressions. The dotted line denotes a shallow dome. The elevation profile along AA' is shown in Figure 9d. (b) A crater destroyed by the linear depression (TC image: TCO\_MAPm04\_N42E300N39E303SC). (c) A putative volcanic cone in a rimless depression (LRO NAC stamp: M1158118841R). (d) Elevation profile along AA' (TC DTM: DTM\_MAP\_02\_N42E300N39E303SC).

Imbrium impact. However, *Campbell et al.* [2009] noted that their trending direction is radial to Iridum crater rather than Imbrium basin and interpreted them as deposits of Iridum ejecta materials.

The other type of linear depression is a single structure located in the eastern part of Mons Rümker (Figure 2). It is a wide linear depression that is about 27 km long, 2–3 km wide, and a few meters to 50 m deep, which is much larger in scale than the first type. This depression is characterized by two elevated rims bounding a relatively flat floor (Figures 9a and 9d). The depression extends from near the center of the Rümker plateau to the eastern margin of Mons Rümker and is buried by the surrounding mare units. It intersects a wrinkle ridge (Figure 9a) and crosscuts several old craters (Figure 9b). In addition, volcanic features such as a shallow dome and a putative volcanic cone [Farrand et al., 2015] are located on the linear depression (Figure 9c), which indicates this type of linear depression may have a volcanic origin.

### 2.2.5. Rilles

In the Mons Rümker region, there is no large lunar rille such as Vallis Schröteri on the Aristarchus plateau [Chevrel et al., 2009], but numerous small sinuous rilles are apparent in high-resolution imagery. These rilles are usually less than 3 km long and 100 m wide (Figure 10a). Most originate from the top of the marginal scarps of the Rümker plateau and extend downward, which indicates that they formed when lava flowed down the scarps and eroded the substrate [Hurwitz et al., 2012]. The largest rille in the region (Figure 10b) is located on the southern marginal scarp of Mons Rümker. It is about 10 km long and is ~500 m across at its widest. It originates from the base of a volcanic dome and fills a crater on its route. The terminal part of the rille is connected to a wrinkle ridge.

## 3. Compositional Analyses

### 3.1. TiO<sub>2</sub> and FeO Contents

TiO<sub>2</sub> and FeO contents of the Mons Rümker region are estimated utilizing the Multiband Imager (MI) data. MI is a high-resolution multispectral imaging instrument on board SELENE. It has five visible (VIS) bands (415 nm, 750 nm, 900 nm, 950 nm, and 1000 nm) and four near-infrared bands (1000 nm, 1050 nm, 1250 nm, and 1550 nm). The VIS bands of MI have the same center wavelengths as those of the Clementine UV/VIS camera but have much higher spatial resolution (20 m/pixel) [Kodama et al., 2010].

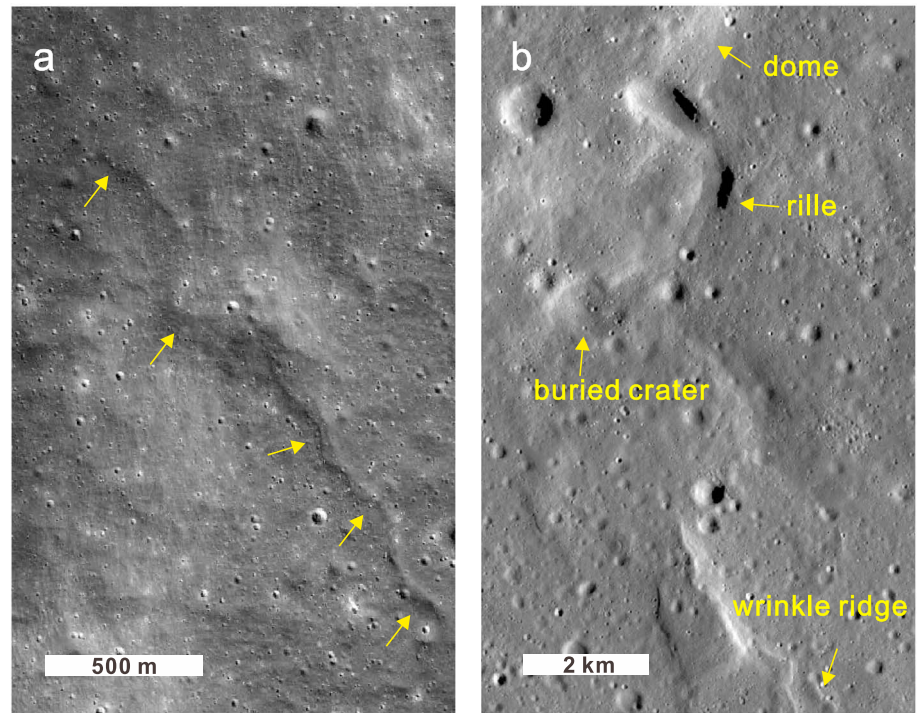


**Figure 10.** Sinuous rilles on the Rümker plateau. (a) A narrow rille (indicated by yellow arrows) on the western marginal scarp of Mons Rümker (central coordinates: 300.22°E, 40.73°N, LRO NAC stamp: M168590433LE). (b) The largest rille in the Mons Rümker region (central coordinates: 301.67°E, 39.67°N, TC image: TCO\_MAPm04\_N42E300N39E303SC).

Otake *et al.* [2012] proposed an algorithm to estimate the TiO<sub>2</sub> and FeO contents:

$$\theta_{Ti} = \arctan\left\{\frac{[(R_{415}/R_{750}) - 0.208]}{[R_{750} - (-0.108)]}\right\} \quad (1)$$

$$\text{wt\%TiO}_2 = 0.72 \times \theta_{Ti}^{14.964} \quad (2)$$

$$\theta_{Fe} = -\arctan\left\{\frac{[(R_{950}/R_{750}) - 1.250]}{[R_{750} - 0.037]}\right\} \quad (3)$$

$$\text{wt\%FeO} = 20.527 \times \theta_{Fe} - 12.266 \quad (4)$$

where  $R_{415}$ ,  $R_{950}$ , and  $R_{750}$  are reflectance of MI data at 415 nm, 950 nm and 750 nm, respectively.  $\theta_{Fe}$  and  $\theta_{Ti}$  are angle parameters related to FeO and TiO<sub>2</sub> abundances. The standard deviations of FeO and TiO<sub>2</sub> abundances derived from the algorithm are 0.81 wt % and 0.43 wt %, respectively [Otake *et al.*, 2012].

The TiO<sub>2</sub> and FeO content maps of the Mons Rümker region are shown in Figure 11. The Rümker plateau features lower TiO<sub>2</sub> and FeO contents (Figure 11) compared with the surrounding mare units (average TiO<sub>2</sub> and FeO contents are 4 wt % and 17 wt %, respectively) [Otake *et al.*, 2012]. The TiO<sub>2</sub> content of Mons Rümker is 1–3 wt %, and the northeastern part (indicated by white dashed lines in Figure 11a) has lower TiO<sub>2</sub> content (1–2 wt %) than the rest of the Rümker plateau (mostly 2–3 wt %). The FeO content of the plateau varies from 10 wt % to 18 wt %. The southern part has higher FeO content (15–17 wt %), especially in some fresh impact craters (17–17.5 wt %), while the northeastern part exhibits lower FeO contents (mostly 13–15 wt %). The lowest FeO content occurs in a deep impact crater (indicated by the black arrow in Figure 11b) in northern Mons Rümker, which is as low as 10 wt %.

### 3.2. Mineral Types

We use the Moon Mineralogy Mapper ( $M^3$ ) data to analyze the mineral composition of the Mons Rümker region.  $M^3$  is a push-broom imaging spectrometer on board India's Chandrayaan-1 lunar orbiter mission [Pieters *et al.*, 2009]. It collected continuous spectra from 430 to 3000 nm between 18 November 2008 and

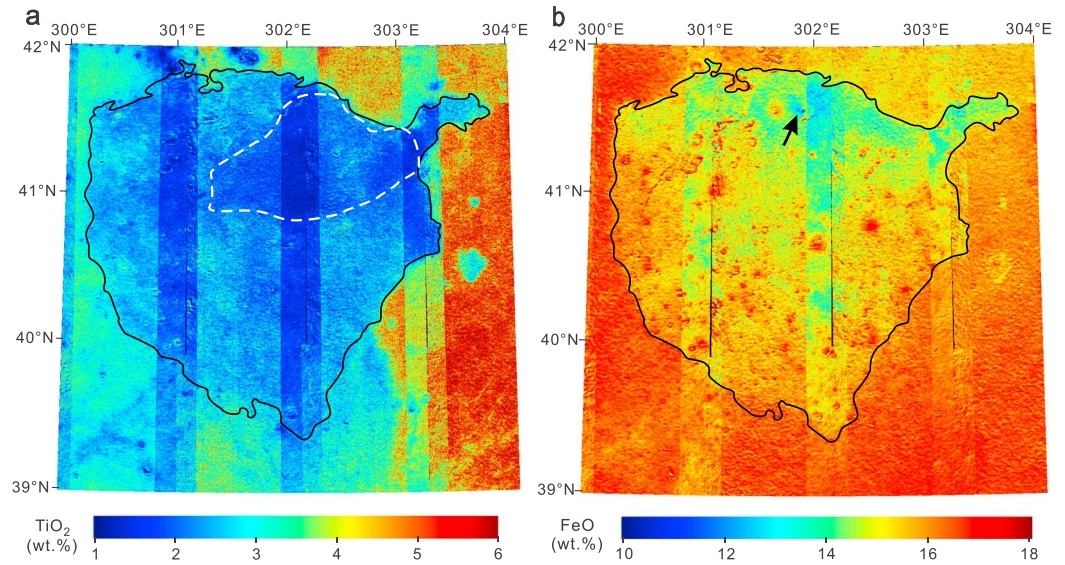


**Figure 11.** (a) TiO<sub>2</sub> and (b) FeO contents of the Mons Rümker region derived from MI data [Otake *et al.*, 2012]. The white dashed line in Figure 11a denotes the area with relatively low TiO<sub>2</sub> content. The black arrow in Figure 11b indicates the crater with lowest FeO content. The black solid lines indicate the boundary of Mons Rümker.

16 April 2009. In the optical period 1B operation phase, the M<sup>3</sup> spectrometer mapped the lunar surface at 140 m/pixel resolution in 85 spectral channels [Pieters *et al.*, 2009]. In this work, the M<sup>3</sup> level 2 reflectance data archived at NASA Planetary Data System (PDS) were used to perform compositional analyses. These data sets have been photometrically and thermally corrected [Isaacson *et al.*, 2013].

To characterize fundamental mineralogical properties (e.g., mafic silicates, soil maturity, and space weathering) of the lunar surface, we calculated the integrated band depth (IBD) at 1000 and 2000 nm from M<sup>3</sup>. The shapes and positions of these bands vary according to the crystallographic position of Fe<sup>2+</sup> in olivine, pyroxene, and spinel [Besse *et al.*, 2011; Mustard *et al.*, 2011; Pieters *et al.*, 2011]. The algorithms for IBD 1000 and IBD 2000 are defined as follows:

$$IBD\ 1000 = \sum_{n=1}^{26} \left( 1 - \frac{R(789 + 20n)}{Rc(789 + 20n)} \right) \quad (5)$$

$$IBD\ 2000 = \sum_{n=1}^{21} \left( 1 - \frac{R(1658 + 40n)}{Rc(1658 + 40n)} \right) \quad (6)$$

where  $R$  is the reflectance at a given wavelength,  $Rc$  refers to the continuum reflectance value (continuum is defined as a slope line across the absorption band), 789 and 1658 are the starting wavelength in nanometer, 20 and 40 are the spectral sampling interval in nanometer, and  $n$  is the number of bands to be covered by the absorption features [Mustard *et al.*, 2011].

A color composite map produced by assigning M<sup>3</sup> IBD 1000 as red, IBD 2000 as green, and 1.58 μm reflectance as blue can be used to present the distribution and type of minerals [Mustard *et al.*, 2011]. Pyroxenes usually show yellow in the color composite map due to the diagnostic absorption features near 1 and 2 μm. Specifically, low-calcium pyroxenes (orthopyroxenes) have 1 μm absorption feature ranging from 0.9 to 0.93 μm and 2 μm absorption feature from 1.8 to 2.1 μm, whereas high-calcium pyroxenes (clinopyroxenes) have absorptions at 0.91–1.07 μm and 1.97–2.36 μm, respectively [Cloutis and Gaffey, 1991]. Olivine exhibits a broad absorption near 1.05 μm but has no absorption near 2 μm, which results in a red color in the map [Sunshine *et al.*, 1990; Sunshine and Pieters, 1998; Horgan *et al.*, 2014]. Plagioclase feldspar often has a broad absorption feature around 1.2 μm due to the substitution of Fe<sup>2+</sup> for Ca<sup>2+</sup> [Ohtake *et al.*, 2009; Cheek *et al.*, 2013; Carter and Poulet, 2013; Wray *et al.*, 2013; Horgan *et al.*, 2014]. However, this absorption feature is generally very weak and can be overwhelmed by minor amounts of pyroxene or olivine, as the

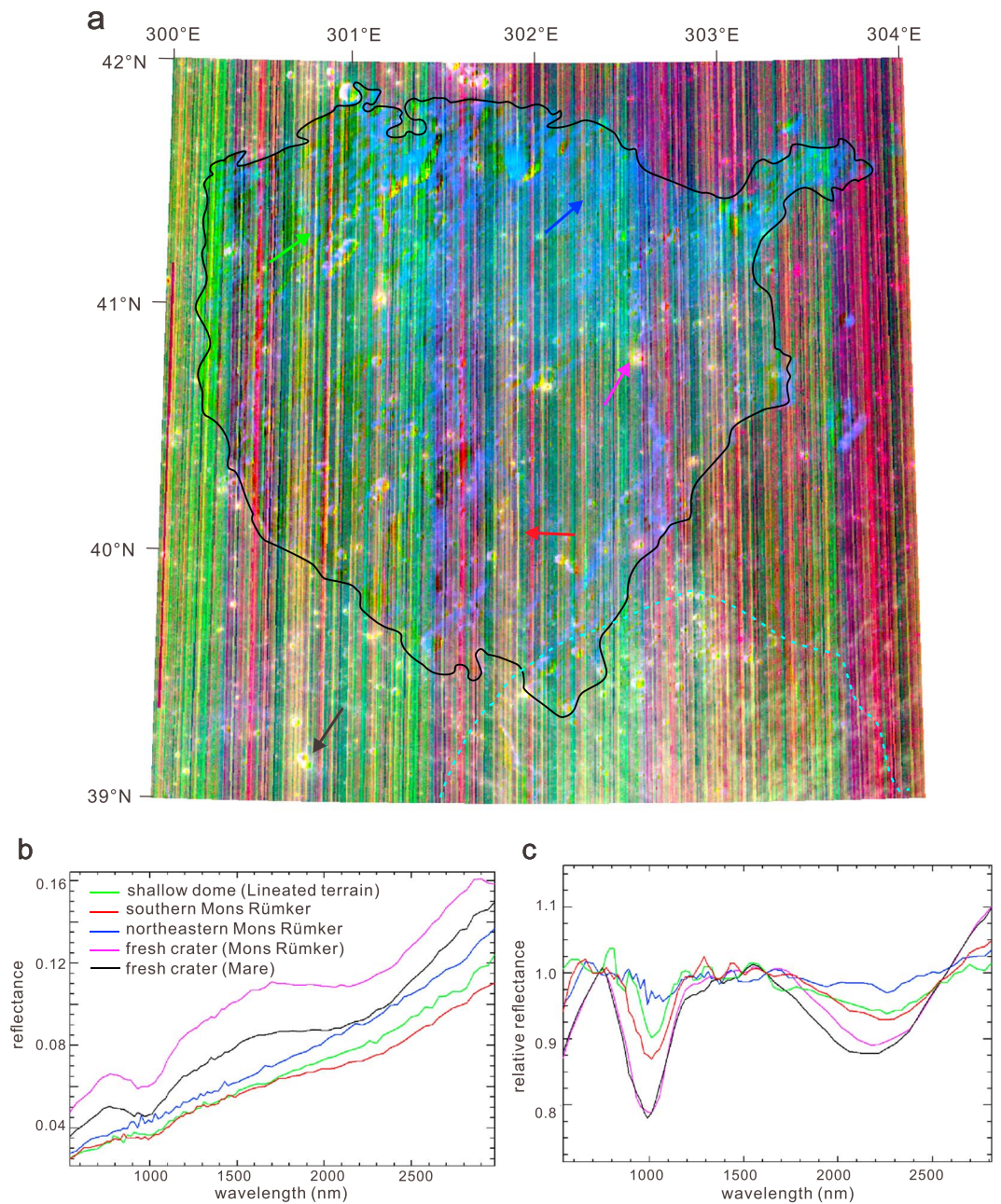


**Figure 12.** (a)  $M^3$  color composite map of the Mons Rümker region produced by assigning IBD 1000 as red, IBD 2000 as green, and  $1.58 \mu\text{m}$  reflectance as blue. The black solid line indicates the boundary of Mons Rümker. The area outlined by the blue dashed line is the ejecta curtain of Rümker E crater. (b)  $M^3$  reflectance spectra extracted from the area pointed by arrows with corresponding colors in Figure 12a. (c)  $M^3$  continuum-removed spectra of the same spots.

iron content in feldspar is low. Therefore, plagioclase feldspar usually shows blue in the composite map. It should be noted that color composite map is just a reference for the estimation of mineral distribution as some other factors may also affect the color in the map. For example, space weathering can lead to lower albedo and weaker absorption depth [Pieters et al., 2000; Hapke, 2001; Noble et al., 2007]. Therefore, it is necessary to combine the IBD analysis and spectral analysis to obtain reliable results on the mineral types.

The color composite map of the Mons Rümker region is shown in Figure 12a. In this map, the southern part of Mons Rümker appears reddish yellow, which indicates a pyroxene-dominated composition but with relatively weak absorptions at both the  $1 \mu\text{m}$  and  $2 \mu\text{m}$  bands due to space weathering [Pieters et al., 1994]. By contrast,

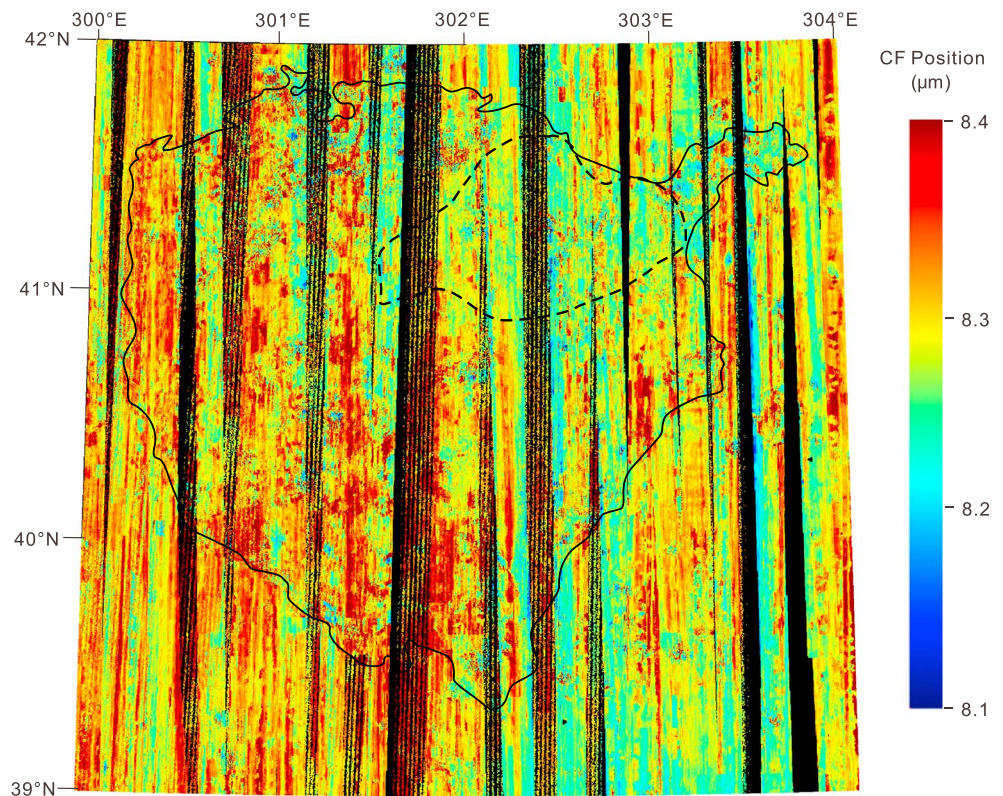


**Figure 13.** Diviner Christiansen Feature (CF) position map of the Mons Rümker region. The black dashed line denotes the area with relatively low CF values. The black solid line indicates the boundary of Mons Rümker.

fresh craters in this area are bright yellow, indicating strong absorptions at both 1  $\mu\text{m}$  and 2  $\mu\text{m}$ . In the southeastern part of the map, crater rays and ejecta curtain (outlined by blue dashed line) of Rümker E crater (out of the map; Figure 1) also show bright yellow. The northeastern part of Mons Rümker is bluish, indicating very weak or absent 1  $\mu\text{m}$  and 2  $\mu\text{m}$  absorption bands, probably due to the existence of highland materials or heavier space weathering [Mustard *et al.*, 2011; Kaur *et al.*, 2013]. We also analyzed the spectra of the northeastern and southern plateau surface, and two representative spectra are shown in Figure 12. Both of them are mean spectra of a  $3 \times 3$  pixel area, and they both show absorptions around 1.0 and 2.25  $\mu\text{m}$  (Figures 12b and 12c), which indicates that high-calcium pyroxene (clinopyroxene) is widely distributed on the surface of Mons Rümker (Figures 12b and 12c). However, in the northeastern part, the weak absorptions near 1  $\mu\text{m}$  and 2.25  $\mu\text{m}$  indicate that high-calcium pyroxene is probably mixed with highland materials. We also analyzed the spectra of fresh craters in both the southern part of Mons Rümker and the southwestern mare, and the spectra of two typical craters are shown in Figures 12b and 12c. Both of them have similar strong absorptions around 1.0  $\mu\text{m}$  and 2.2  $\mu\text{m}$ , indicating that they are similarly dominated by high-calcium pyroxene. In addition, the spectrum of a shallow dome (dome No. 17) in the lineated terrain (Figures 12b and 12c) also indicates similar high-calcium pyroxene dominated composition.

### 3.3. Bulk Silicate Mineralogy

The Diviner Lunar Radiometer Experiment is a multispectral radiometer on board LRO. It has variable spatial resolution that depends on orbital altitude and has nine spectral channels covering the  $\sim 0.3$ –400  $\mu\text{m}$  wavelength range [Paige *et al.*, 2010]. The three “8  $\mu\text{m}$ ” channels centered at 7.8, 8.25, and 8.55  $\mu\text{m}$  can be used to map the position of Christiansen Feature (CF), which is related to silicate polymerization. The CF position occurs at shorter wavelengths for felsic and feldspathic compositions and longer wavelengths for mafic compositions [Logan *et al.*, 1973; Salisbury and Walter, 1989; Lawrence *et al.*, 2013]. Therefore, it is a compositional indicator of silicate mineralogy and is helpful for the analysis of formation mechanism of lunar domes

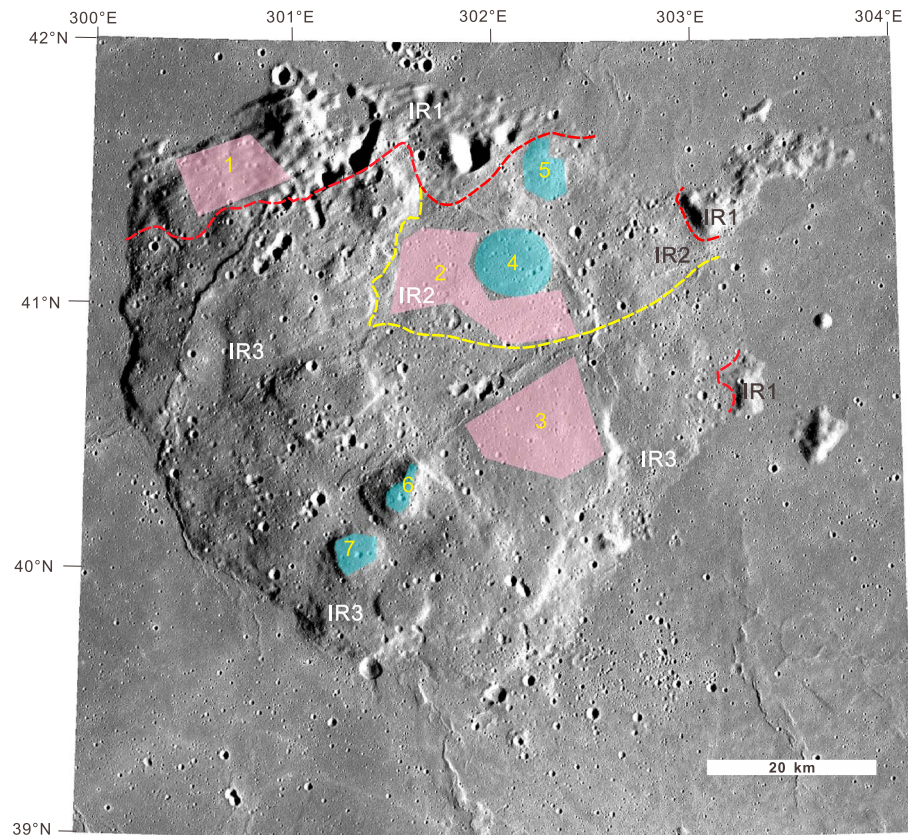


**Figure 14.** Boundaries of plateau-forming units on the Rümker plateau showed on TC images (image ID: TCO\_MAPm04\_N42E300N39E3035C and TCO\_MAPm04\_N42E303N39E3065C). Red dashed lines are the borders of unit IR1. The yellow dashed line denotes the boundary between unit IR2 and IR3. Numbers denote regions where we performed crater counting (pink and cyan areas belong to plateau-forming units and dome units, respectively).

[Glotch *et al.*, 2010, 2011; Greenhagen *et al.*, 2010; Jolliff *et al.*, 2011; Lawrence *et al.*, 2013; Ashley *et al.*, 2016]. For this study, we generated a 256 pixel per degree CF map (Figure 13) corrected for solar incidence angle and normalized to equatorial values at noon according to the methods of Greenhagen *et al.* [2010] and the estimated error of a CF measurement is  $\sim 0.02 \mu\text{m}$ .

About 90% of the Mons Rümker region has CF positions ranging from 8.2 to 8.4  $\mu\text{m}$ , consistent with a basaltic composition (Figure 13) [Greenhagen *et al.*, 2010]. Therefore, the surface of Mons Rümker is mainly covered by basaltic materials which have relatively low  $\text{SiO}_2$  contents. Some fresh craters and a few locations in the northeastern part have CF positions at 8.1–8.2  $\mu\text{m}$  (Figure 13), potentially indicating the existence of slightly more felsic materials [Greenhagen *et al.*, 2010]. However, it is also possible that lower CF values of some fresh craters could result from low maturity [Lucey *et al.*, 2010, 2017; Glotch *et al.*, 2015] as their spectra exhibit obvious pyroxene absorption features (Figures 12b and 12c). In addition, the northeastern Rümker plateau (denoted by black dashed line in Figure 13) has CF positions around 8.25  $\mu\text{m}$ , which is relatively lower compared with the rest areas on the plateau. It indicates that this area has elevated  $\text{SiO}_2$  contents, though it is dominated by basaltic materials [Greenhagen *et al.*, 2010]. Domes on the Rümker plateau also have CF positions at 8.2–8.4  $\mu\text{m}$  and do not show obvious differences in CF values with their surrounding regions.

#### 4. Age Determination

Mons Rümker is embayed by an Imbrian mare unit (3.47 Ga) [Hiesinger *et al.*, 2003] to the west and an Eratosthenian mare unit (1.33 Ga) [Hiesinger *et al.*, 2003] to the east. Therefore, the Mons Rümker plateau could have been formed before 3.47 Ga ago. To estimate the absolute model ages of the plateau surface,

**Table 2.** Dating Results of the Investigated Units

Region <sup>a</sup>	Count Area (km <sup>2</sup> )	Number of Counted Craters	$N(1)$ (km <sup>-2</sup> )	Absolute Model Age (Ga)	Unit
1	73.958	219	0.01080	3.71 (+0.04/-0.05)	IR1
2	134.621	532	0.00614	3.58 (+0.03/-0.04)	IR2
3	126.416	474	0.00490	3.51 (+0.04/-0.06)	IR3
4	56.069	214	0.00523	3.53 (+0.06/-0.09)	shallow dome
5	22.706	61	0.00406	3.43 (+0.11/-0.46)	shallow dome
6	11.871	51	0.00263	3.04 (+0.31/-0.94)	steep-sided dome
7	21.155	76	0.00247	2.91 (+0.42/-0.99)	steep-sided dome

<sup>a</sup>Regions for crater counting are shown in Figure 14.

we have identified three plateau-forming units (outlined on Figure 14 and named as IR1, IR2, and IR3, respectively) based on the spectral properties and geomorphologic characteristics. The first unit (IR1) is the lineated terrain in the northern part of Mons Rümker. It is distinct in morphology which features NEE trending linear depressions with smooth materials that could be ejecta of Iridum impact partly overlaid by a thin layer of basaltic materials [Scott and Eggleton, 1973; Smith, 1974; Campbell et al., 2009]. The second unit (IR2) occupied the northeastern Rümker plateau. It features rough surface, higher density of secondary crater clusters and lower CF values, and TiO<sub>2</sub> contents compared to the surrounding areas. The northern part of this unit superposed on the linear depressions (Figure 2d), which indicates unit IR2 is younger than IR1. The unit IR3 is the most widely distributed basalt unit in Mons Rümker. It also has rough surface but has higher TiO<sub>2</sub> and FeO contents and CF values compared with unit IR2. We performed crater size-frequency distribution (CSFD) measurements [Michael and Neukum, 2010] on these three units and got absolute model ages of 3.71 Ga for IR1, 3.58 Ga for IR2, and 3.51 Ga for IR3 (Table 2 and Figure 15) based on the production function and cratering chronology model proposed by Neukum et al. [2001].

We also tried to acquire the model ages of domes in order to better constrain the duration of volcanic activity on the Rümker plateau. However, some domes have very small surface areas, which lead to large errors in the dating result. In addition, widely distributed secondary craters could also make the result unreliable. Therefore, we chose two steep-sided domes (dome No. 2 and No. 6) and two shallow domes (dome No. 16 and No. 21) that have relatively larger area and fewer secondary craters to perform CSFD measurements. The general trends of their best fit model ages (Table 2 and Figure 16) show that steep-sided domes (2.91 Ga for No. 2 and 3.04 Ga for No. 6) could be younger than shallow domes (3.53 Ga for No. 16 and 3.43 Ga for No. 21).

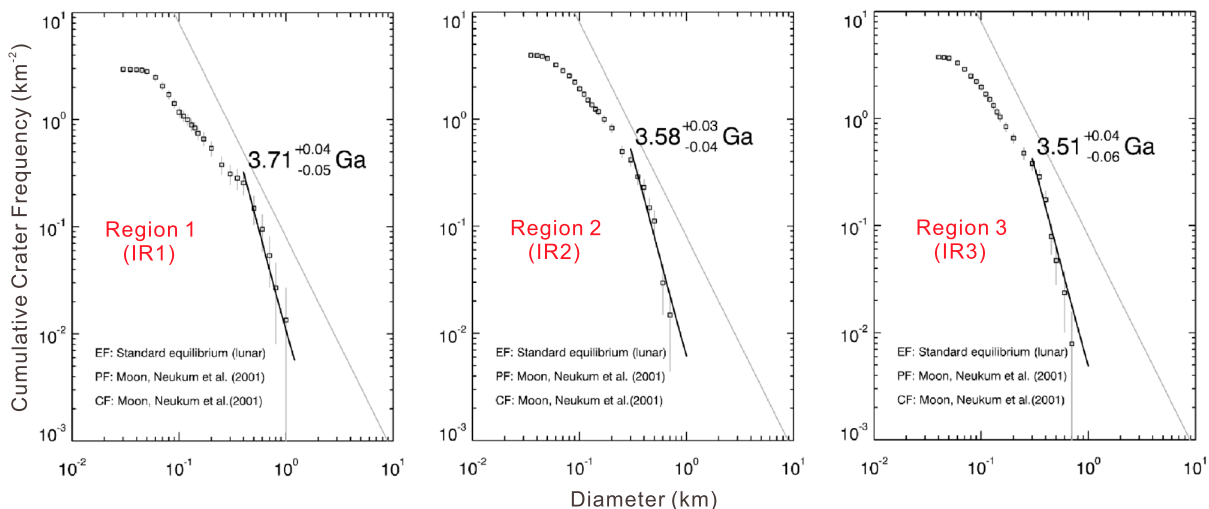


**Figure 15.** Cumulative crater size-frequency distributions and absolute model ages of plateau-forming units on the Rümker plateau.

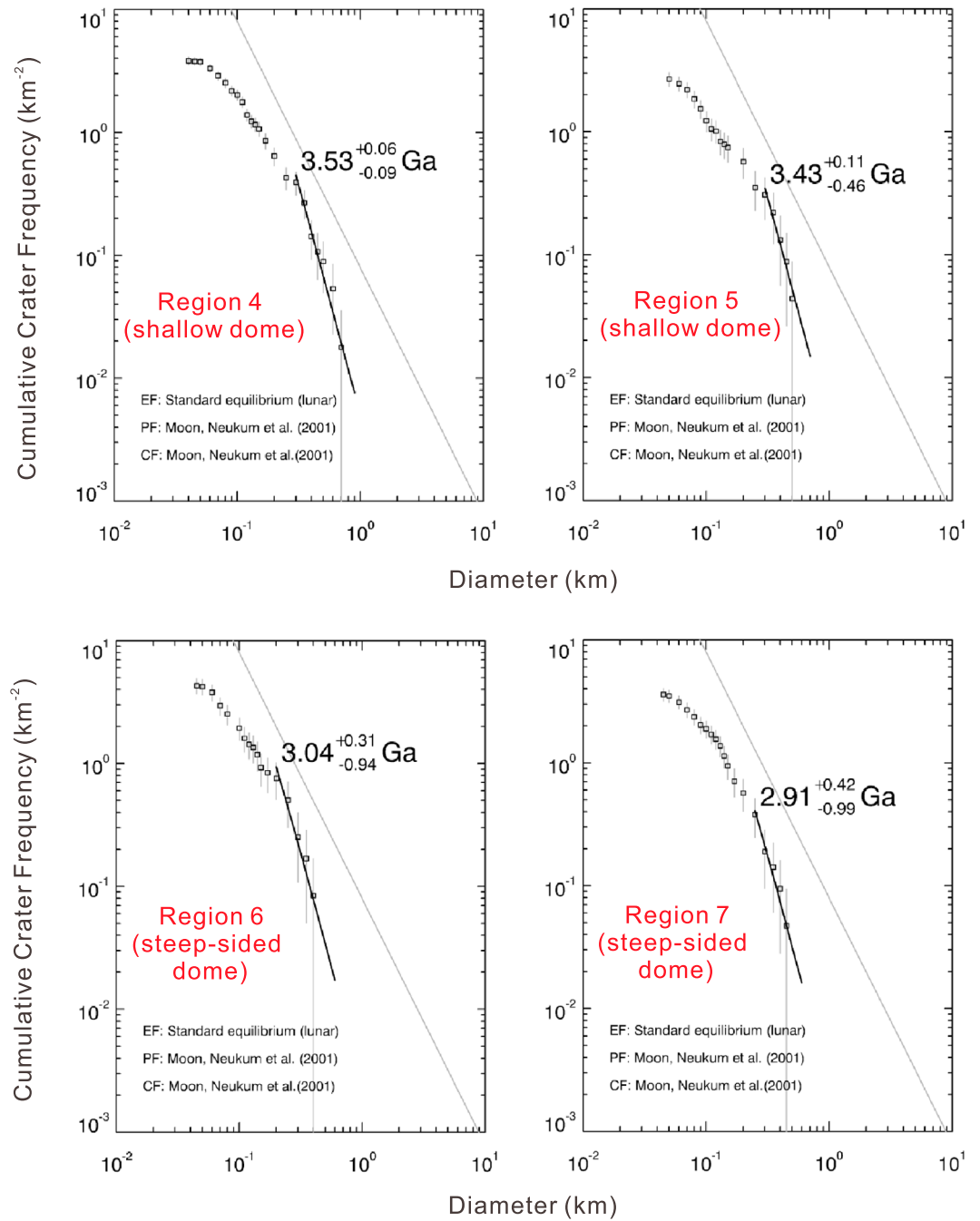


**Figure 16.** Cumulative crater size-frequency distributions and absolute model ages of domes on the Rümker plateau.

**5. Discussions**

**5.1. Composition of Mons Rümker**

Spectral data from M<sup>3</sup> reveals that the dominant mafic mineral on the Rümker plateau is high-calcium pyroxene which has diagnostic absorption features at 1.0 and 2.15 μm. Pyroxene is the major mafic mineral of basalt. According to the FeO and TiO<sub>2</sub> content (~15 wt % and ~1.5 wt % in average, respectively), we can infer that the main rock type on the Rümker plateau is low-Ti basalt [Neal and Taylor, 1992].

However, highland materials may also exist on the Rümker plateau. The average FeO content of lunar mare basalt is ~16 wt % [Jolliff et al., 2000; Lawrence et al., 2002; Gillis et al., 2004], which is higher than the

northeastern Rümker plateau (~14 wt % in average and as low as 10%). As highland materials are mainly composed of plagioclase feldspar that has low FeO content (~4.5 wt % in average) [Gillis *et al.*, 2004], the lower FeO content of northeastern Mons Rümker could result from the mixing of highland and basaltic materials [Jolliff *et al.*, 2000]. Similarly, Diviner data show that the CF positions of the northeastern Rümker plateau (mostly 8.20–8.30  $\mu\text{m}$ , Figure 13) are located between the average CF values of lunar highland and mare (8.15 and 8.30  $\mu\text{m}$ , respectively) [Greenhagen *et al.*, 2010], which also indicate the mixing of basaltic and felsic materials [Greenhagen *et al.*, 2010; Lawrence *et al.*, 2013]. On the  $M^3$  color composite map, this area appears blue that generally indicates the existence of highland materials or heavy space weathering [Mustard *et al.*, 2011; Kaur *et al.*, 2013]. It is unlikely that space weathering leads to the blue color as space weathering would result in higher CF values [Lucey *et al.*, 2010, 2017; Glotch *et al.*, 2015], which is inconsistent with the slightly lower CF values of the northeastern part. Therefore, existence of highland materials could be the main reason. However, the  $M^3$  spectra of this area did not show typical absorption features of feldspar, which could be due to the small percentage of feldspar relative to pyroxene [Cheek *et al.*, 2013; Cheek and Pieters, 2014; Horgan *et al.*, 2014]. Cheek *et al.* [2013] studied the spectra of feldspar and pyroxene mixtures and found that only when feldspar takes up more than 85% can the absorption feature of feldspar be easily observed. This, together with the nonuniform distribution of FeO content in the northeastern part, may indicate that highland materials on Mons Rümker are not in the form of large highland rocks. Instead, they are most likely to be felsic impact ejecta from highland region and are mixed with the basalt on Mons Rümker. This hypothesis is also consistent with the result from geophysical models proposed by Huang *et al.* [2014]. They obtain a porosity of 12% for the Rümker plateau, which is much larger than the porosity of typical lunar basalt samples (~7%). They proposed that mixture of igneous rocks and highland materials probably occurs in Mons Rümker [Huang *et al.*, 2014]. In addition, morphologic analyses also provide supportive evidence for the hypothesis. The northeastern Rümker plateau has a high density of secondary crater clusters (Figure 2), and most of them could be formed by the ejecta of Pythagoras crater that is located in the highland region to the north of Oceanus Procellarum. Therefore, ejecta of the Pythagoras crater could be the source of highland materials in northeastern Rümker plateau.

The existence of pyroclastic deposits has been proposed in previous studies [Campbell *et al.*, 2009; Farrand *et al.*, 2015]. However, they did not provide compelling evidences. Pyroclastic deposits have been thought to form the dark-mantle deposits on the lunar surface which are characterized by low albedo, smooth surface, and mantling relationships to underlying terrain features [Adams *et al.*, 1974; Head, 1974; Heiken *et al.*, 1974; Gustafson *et al.*, 2012]. Pyroclastic deposits are widely distributed on lunar surface and are often observed near the highland/mare boundary or associated with fissures within floor-fractured craters [Gustafson *et al.*, 2012; Gaddis *et al.*, 2003; Jozwiak *et al.*, 2012]. They usually have high FeO contents and widely varying  $\text{TiO}_2$  contents [Campbell *et al.*, 2008; Gaddis *et al.*, 2003]. Spectra of volcanic glasses in the pyroclastic deposits also have 1 and 2  $\mu\text{m}$  band absorption features. However, compared with pyroxene, the absorptions of volcanic glasses are broader and shallower, and the 1 and 2  $\mu\text{m}$  band centers are generally shifted to longer and shorter wavelength, respectively [Adams and McCord, 1971; Bell *et al.*, 1976; Besse *et al.*, 2014; Jawin *et al.*, 2015]. For example, laboratory spectra of orange volcanic glasses from lunar samples have 1  $\mu\text{m}$  band absorption features at 1.05–1.2  $\mu\text{m}$  and 2  $\mu\text{m}$  band at 1.9–2.05  $\mu\text{m}$  [Besse *et al.*, 2014]. On the Rümker plateau, we did not find obvious morphologic features such as low albedo mantle deposits that may be associated with pyroclastic deposits. In addition, analyses on the  $M^3$  spectra suggested that both the volcanic domes that could be the source of pyroclastic materials and the plateau surface did not show typical absorption features of volcanic glasses (Figures 12b and 12c). Therefore, pyroclastic deposits likely do not exist on the Rümker plateau.

## 5.2. Formation Mechanism of the Domes on the Rümker Plateau

Lunar domes have been classified into extrusive and intrusive domes based on their origins [Head and Gifford, 1980; Wöhler and Lena, 2009]. An extrusive dome usually forms when magma with high-viscosity and/or low effusion rate erupts and accumulates around the effusive vent, while intrusive domes are usually formed by flexure and lifting of surface strata resulting from a near-surface magmatic intrusion [Wöhler and Lena, 2009].

In the Mons Rümker region, the steep-sided domes have distinct contacts with the surrounding plains and all of them have volcanic features, indicating that they are extrusive domes formed by higher-viscosity magma and/or low effusion rates [Head *et al.*, 1978; Weitz and Head, 1999]. Generally, magma viscosity would increase

with higher silica content, lower magma temperature, and higher crystal content [Head *et al.*, 1978; Basaltic Volcanism Study Project, 1981; Schmincke, 2004; Wöhler *et al.*, 2006, 2007b]. Determining what factors lead to steep flank slopes will help us better understand the magma property of Mons Rümker volcanism. On the lunar surface, steep-sided domes are concentrated near the mare/highland boundary of Mare Imbrium (Gruithuisen Domes and Mairan Domes) [Head *et al.*, 1978; Chevrel *et al.*, 1999; Wagner *et al.*, 2002; Wilson and Head, 2003; Glotch *et al.*, 2011; Ivanov *et al.*, 2016], in Mare Cognitum (Hansteen  $\alpha$ ) [Wagner *et al.*, 2010], and on volcanic plateaus of Oceanus Procellarum (Marius Hills, Mons Rümker) [Smith, 1974; Weitz and Head, 1999; Heather *et al.*, 2003; Huang *et al.*, 2011; Lawrence *et al.*, 2013]. Gruithuisen domes (including Gruithuisen  $\delta$  and Gruithuisen  $\gamma$ ) are located in the northwestern border of Mare Imbrium [Chevrel *et al.*, 1999]. Their diameters are 21.6 and 25.1 km, respectively, and have mean flank slopes of 13.1° and 12.0°, respectively [Chevrel *et al.*, 1999; Ivanov *et al.*, 2016]. Gruithuisen domes are among the lunar red spots that are characterized by high albedo, strong UV absorption, and a wide range of morphologies [Wagner *et al.*, 2002]. They also feature lower TiO<sub>2</sub> (~1 wt %) and FeO (5–8 wt %) contents and low CF value (<7.0 in some cases), which suggests that Gruithuisen domes consist of high-silica rocks such as rhyolite or quartz monzonite [Kusuma *et al.*, 2012; Ivanov *et al.*, 2016]. The Mairan domes and Hansteen  $\alpha$  are also lunar red spots that have large flank slopes, low TiO<sub>2</sub> and FeO contents, and low CF values, which are similar as Gruithuisen domes [Wilson and Head, 2003; Wagner *et al.*, 2010; Glotch *et al.*, 2010, 2011]. For these steep-sided domes, high silica content is the main factor leading to the formation of steep flanks [Wilson and Head, 2003; Ivanov *et al.*, 2016]. Unlike the domes discussed above, steep-sided domes in Marius Hills are different in morphologic and compositional characteristics. These domes have smaller diameters (usually several kilometers) and smaller flank slopes (5–10°) [Weitz and Head, 1999; Lawrence *et al.*, 2013]. They have rough surfaces and lower surface albedo, high TiO<sub>2</sub> (5–9 wt %) and FeO content (15–19 wt %), and low silica content [Heather *et al.*, 2003; Lawrence *et al.*, 2013]. Therefore, Lawrence *et al.* [2013] proposed that low eruption temperature, high crystal content, and low eruption rates result in the formation of steep-sided domes in Marius Hills. In the Mons Rümker region, steep-sided domes have much smaller diameters (2–11 km in average) and flank slopes (5–10°) than the Gruithuisen domes. They have basaltic composition with relatively high FeO content (15–18 wt %) and CF values (around 8.3), indicating a low silica content. There is a possibility that the domes are formed by silicic materials and then covered by basaltic ejecta. However, fresh impact craters on the domes also show high FeO content and pyroxene-dominant spectral feature. Therefore, steep-sided domes in Mons Rümker are most similar as the domes in Marius Hills and lower eruption temperature and higher crystal content could be the main factors increasing the viscosity of magma. Moreover, absolute model ages of these steep-sided domes show that they are younger than the plateau-forming materials. Taking these factors into consideration, the steep-sided domes could be formed by relatively cool, high-viscosity magma in the terminal stage of volcanic activity when the effusion rate was low.

Compared with steep-sided domes that are only observed in several areas on the lunar surface, shallow domes with flank slopes less than 5° are more common and most of them are effusive domes formed when the viscosity of magma increases and the effusion rate decreases [Head and Gifford, 1980; Weitz and Head, 1999; Lawrence *et al.*, 2013]. On the Rümker plateau, most of the shallow domes show features of lava accumulation or superposition on surrounding plateau surface (Figures 7g and 7h), which provide evidences for an effusive origin. However, these features were not identified on dome No. 16 (Figure 7c), which could be due to an intrusive origin of the dome or low-viscosity magma erupting on preexisting positive topography. Wöhler and Lena [2009] studied some intrusive domes on lunar surface based on telescope observations and proposed that intrusive domes usually have low flank slopes (less than 1°), large diameters (usually 10–20 km and can be larger than 30 km), regular but noncircular outline, and lack summit pits. Besides, tensional features such as faults and linear rilles could be found near the intrusive domes [Wöhler and Lena, 2009; Wöhler *et al.*, 2010]. The dome No. 16 is not consistent with most of these criteria and may not be an intrusive dome, although this possibility cannot be ruled out. It is more likely that the dome No. 16 is an effusive dome formed by magma erupting on preexisting positive topography. This dome and its surrounding plateau unit IR2 have homogeneous compositions and close absolute model ages. In addition, the dome is located near the center of the unit IR2 and occupies the highest region in this unit (Figures 6 and 14). Therefore, the dome No. 16 may be the source region of the lava forming unit IR2. In summary, shallow domes in Mons Rümker could also be effusive in origin. As the shallow domes and steep-sided domes on Mons Rümker have similar compositions, their differences on morphology imply variations in the physical properties and eruption

conditions of magma during different stages of Mons Rümker volcanic activity. Shallow domes formed when magma started to cool down and effusion rate decreased. Absolute model ages show that they are contemporary or a little later than the volcanic event forming plateau surface unit IR2 and IR3. Then with time, magma became cooler and the effusion rate was lower, which lead to the formation of steep-sided domes.

### 5.3. Geologic Evolution of the Mons Rümker Region

Analyses of the geomorphology, composition, and absolute mode ages of the Mons Rümker region have revealed the complicated geologic history of this area. In this study, at least four stages of volcanic activities are identified on the Rümker plateau. The first stage ended around 3.71 Ga and the lava partly covered the linear depressions that could be formed by ejecta from Iridium impact. Stage 2 occurred around 3.58 Ga, and the lava features lower TiO<sub>2</sub> content (1–2%) and superposed on part of the linear depressions in IR1 unit. Stage 3 occurred around 3.51 Ga and covers the central and southern part of the plateau. Compared with stage 2, basalt formed in this stage features elevated TiO<sub>2</sub> (mostly 2–3%) and FeO content (15–17%). The last stage is the formation of steep-sided domes around 3 Ga. These domes are younger than the basalt in unit IR3 even if taking the error bars into consideration. Their compositions are similar with the plateau-forming materials.

A new geologic map of the Mons Rümker region (Figure 17) has been produced by synthesizing the results in this study. We also proposed a possible scenario for the geologic evolution of the Mons Rümker region:

1. Ejecta of Iridium impact formed the lineated terrain in the northern part of Mons Rümker before 3.71 Ga.
2. Volcanic activity on the Rümker plateau at about 3.71 Ga, 3.58 Ga, and 3.51 Ga formed the basalt units IR1, IR2, and IR3, respectively.
3. Shallow domes (ld) formed around 3.5 Ga or slightly younger due to magma extrusion.
4. At about 3.47 Ga, magmatic eruption in Oceanus Procellarum formed the mare unit Im and superposed the outer part of Mons Rümker.
5. In the terminal stage of volcanic activity on the Rümker plateau, steep-sided domes formed and were active until ~3.0 Ga (Eratosthenian).
6. An episode of volcanic activity occurred at about 1.33 Ga in Oceanus Procellarum, and the mare lava superposed the eastern part of the Rümker plateau.

### 5.4. Candidate Landing Sites for Chang'E-5

In the process of landing site selection for a sample return mission, both the engineering constraints and scientific value should be taken into consideration. As the engineering requirements of Chang'E-5 landing site have not been published yet, we use the data of Chang'E-3 mission which is China's first lunar soft-landing mission [Ip *et al.*, 2014; Zhao *et al.*, 2014; Xiao *et al.*, 2015] for reference. Chang'E-3 lander requires a surface slope of less than 8° for the landing site [Sun *et al.*, 2014]. Here we propose two candidate landing sites for sample collection (Table 3).

The first candidate landing site (landing site A, Figures 18a and 18b and Table 3) is located on the top of a steep-sided dome (dome No. 2) with coordinates 301.34°E, 40.11°N. This dome has a relatively flat and broad top with an area of ~16 km<sup>2</sup>. The elevation of the proposed landing site is –1500 m, and the slope is ~2.5° at a baseline length of 30 m, which is flat and safe for the lander. This site is also of high scientific value. By analyzing the composition of rocks, we can determine the silica content, titanium, and iron abundances, which are directly related to the magma viscosity. These, together with the physical properties of the rock (e.g., density and porosity), will provide basic information for rheologic modeling in the analysis of formation mechanism of steep-sided domes on the Rümker plateau and provide references for the study of other volcanic domes on the Moon [Lena *et al.*, 2007, 2008; Wöhler *et al.*, 2007b; Arya *et al.*, 2014]. In addition, as the formation of steep-sided domes may represent the last stage of Mons Rümker volcanism, dating of the rocks will help us better constrain the duration of volcanism in the Mons Rümker region and improve the CSFD dating method.

The other candidate landing site is located in the northern lineated terrain (landing site B, Figures 18c and 18d and Table 3; coordinates: 300.69°E, 41.52°N). The elevation is –2270 m, and the slope is ~1.7° at a baseline length of 30 m. This area could be the oldest unit on the surface of Mons Rümker (IR1, 3.71 Ga), and some confusing problems about this area are still unsolved. First, it has been proposed that this area could be

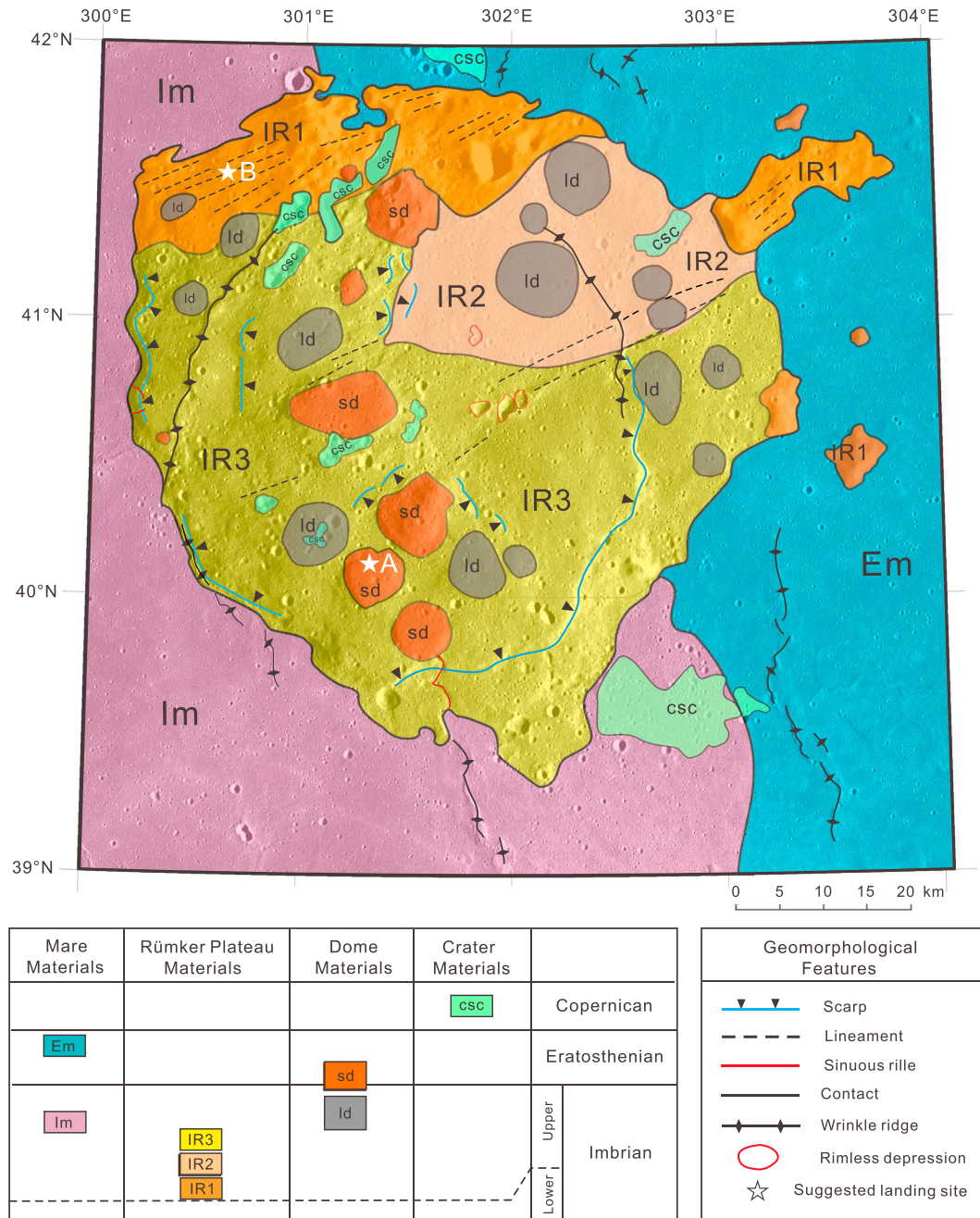


**Figure 17.** Geologic map of the Mons Rümker region. The background is SELENE TC morning map (data ID: TCO\_MAPm04\_N42E300N39E303SC and TCO\_MAPm04\_N42E303N39E306SC).

**Table 3.** Basic Information of the Two Candidate Landing Sites

Landing Site	Coordinates	Elevation (m)	Surface Slope (deg)	Geologic Feature	Scientific Value
A	301.34°E, 40.11°N	-1500	2.5	Steep-sided dome	<ol style="list-style-type: none"> <li>1. Study the origin of lunar domes</li> <li>2. Constrain the duration of Mons Rümker volcanism</li> <li>3. Improve CSFD dating method</li> </ol>
B	300.69°E, 41.52°N	-2270	1.7	Lineated terrain	<ol style="list-style-type: none"> <li>1. Study the origin of lineated terrain</li> <li>2. Check if pyroclastic materials exist</li> <li>3. Determine the age of large impact events on the Moon</li> <li>4. Improve CSFD dating method</li> </ol>

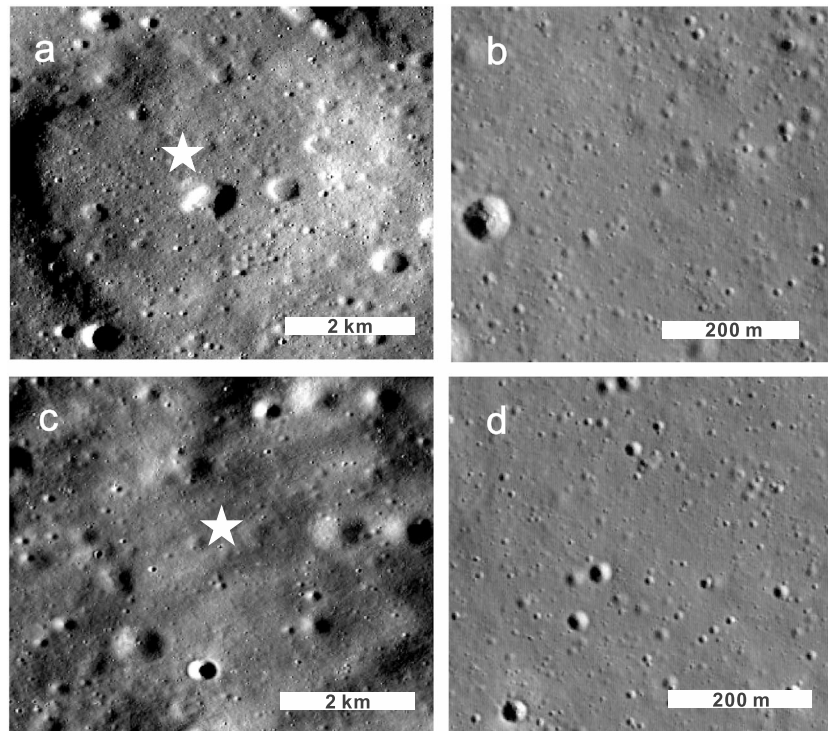


**Figure 18.** Two proposed candidate landing sites (indicated by white stars) for Chang'E-5 mission. (a) TC image of the candidate landing site A (coordinates: 301.34°E, 40.11°N, data ID: TCO\_MAPm04\_N42E300N39E303SC). (b) Close-up view of the candidate landing site A (LRO NAC: M1142838642LE). (c) TC image of the candidate landing site B (coordinates: 300.69°E, 41.52°N, data ID: TCO\_MAPm04\_N42E300N39E303SC). (d) Close-up view of the candidate landing site B (LRO NAC: M1112211163LE).

covered by pyroclastic materials [Campbell *et al.*, 2009; Farrand *et al.*, 2015], while in our study, we did not find typical spectral characteristics of volcanic glass with  $M^3$  data, and there are also no related geomorphologic features such as dark mantle deposits identified. Analyzing the composition of the samples at this site will shed light on this question and also provide us with accurate compositional information on the early stage of Mons Rümker volcanism as it is the oldest unit exposed on the plateau surface. Second, the source of the lineated materials is controversial. These materials have been considered as ejecta of Imbrium impact [Scott and Eggleton, 1973; Smith, 1974] or Iridum impact [Campbell *et al.*, 2009]. Imbrium basin formed around 3.85 Ga according to the dating of Apollo samples [Stöffler and Ryder, 2001], while Iridum basin is younger as it superposed on the northwest of Imbrium basin [Boyce and Dial, 1975; Qiao *et al.*, 2014]. Therefore, dating the samples at site B will help confirm the source of the ejecta. In addition, if the ejecta turn out to be from Iridum impact, the age of Iridum impact will be important for both the improvement of CSFD dating method and the study of lunar geologic history.

## 6. Conclusions

Mons Rümker is a volcanic complex with a complicated geologic history, which makes it a candidate landing region with high scientific value. We studied the geomorphology, mineralogy, and the age of Mons Rümker with multisource remote sensing data. Principal results include the following:

1. The volcanic complex stands up 200–1300 m above the surrounding mare surface, and 75% of the plateau has a slope of less than 3°.
2. A variety of landforms including impact craters, domes, scarps, wrinkle ridges, linear depressions, and sinuous rilles have been observed on the plateau. Among them, domes are the most prominent volcanic landforms and a total of 22 domes have been confirmed with SELENE TC imagery and DTM data. We divided them into steep-sided domes and shallow domes, which may represent different stages of volcanic activities on the Rümker plateau.

3. Spectral analyses indicate that Mons Rümker is mainly covered by low-Ti basalt and the dominant mafic mineral is high-calcium pyroxene. Most of the Mons Rümker region has TiO<sub>2</sub> and FeO contents of 1–3 wt % and 13–17 wt %, respectively. The northeastern part of the plateau exhibits compositional features of mixing of highland and basaltic materials. Domes in Mons Rümker have almost identical compositional characteristics with their surrounding plains and have slightly lower SiO<sub>2</sub> contents.
4. Three main basalt units have been identified on the Rümker plateau, and their absolute model ages are 3.71 Ga, 3.58 Ga and 3.51 Ga, respectively. Volcanic activity may have lasted until the Eratosthenian and steep-sided domes formed in the terminal stage of the volcanic activity. A geologic map has been produced based on these results.
5. Two candidate landing sites have been proposed for the Chang'E-5 mission. By obtaining drill hole samples, we will obtain a better understanding of the Mons Rümker volcanism and the lunar geologic history.

#### Acknowledgments

This study was supported by the National Scientific Foundation of China (41373066 and 11403020) and the State Scholarship Fund (201506410010). The data for crater size-distribution measurements have been included in the supporting information. Other data can be accessed from JMARS (jmars.asu.edu) and PDS (pds.jpl.nasa.gov) with IDs. We thank Zhiyong Xiao for useful discussions. We are grateful to Editor Steven A. Hauck II and two anonymous reviewers for their comments and suggestions that greatly improved our manuscript.

#### References

- Adams, J. B., and T. B. McCord (1971), Alteration of lunar optical properties: Age and composition effects, *Science*, *171*(3971), 567–571, doi:10.1126/science.171.3971.567.
- Adams, J. B., C. Pieters, and T. B. McCord (1974), Orange glass—Evidence for regional deposits of pyroclastic origin on the Moon, *Lunar Planet. Sci.*, Abstract 171–186.
- Arya, A. S., R. P. Rajasekhar, Amitabh, B. Gopala Krishna, Ajai, and A. S. Kiran Kumar (2014), Morphometric, rheological and compositional analysis of an effusive lunar dome using high resolution remote sensing data sets: A case study from Marius hills region, *Adv. Space Res.*, *54*(10), 2073–2086, doi:10.1016/j.asr.2013.10.014.
- Ashley, J., M. Robinson, J. Stopar, T. Glotch, B. R. Hawke, C. van der Bogert, H. Hiesinger, S. Lawrence, B. Jolliff, and B. Greenhagen (2016), The Lassell massif—A silicic lunar volcano, *Icarus*, *273*, 248–261, doi:10.1016/j.icarus.2015.12.036.
- Bell, P., H. Mao, and R. Weeks (1976), Optical spectra and electron paramagnetic resonance of lunar and synthetic glasses—A study of the effects of controlled atmosphere, composition, and temperature, *Lunar Planet. Sci.*, Abstract 2543–2559.
- Besse, S., J. Sunshine, and L. Gaddis (2014), Volcanic glass signatures in spectroscopic survey of newly proposed lunar pyroclastic deposits, *J. Geophys. Res. Planets*, *119*, 355–372, doi:10.1002/2013JE004537.
- Besse, S., J. M. Sunshine, M. I. Staid, N. E. Petro, J. W. Boardman, R. O. Green, J. W. Head, P. J. Isaacson, J. F. Mustard, and C. M. Pieters (2011), Compositional variability of the Marius Hills volcanic complex from the Moon Mineralogy Mapper (M<sup>3</sup>), *J. Geophys. Res.*, *116*, E00G13, doi:10.1029/2010JE003725.
- Boyce, J. M., and A. Dial (1975), Relative ages of flow units in Mare Imbrium and Sinus Iridum, *Lunar Planet. Sci.*, Abstract, 2585–2595.
- Burns, B., and D. Campbell (1985), Radar evidence for cratering on Venus, *J. Geophys. Res.*, *90*(B4), 3037–3047, doi:10.1029/JB090iB04p03037.
- Burrough, P. A., and R. A. McDonnell (1998), *Principles of Geographical Information Systems*, 2nd ed., 356 pp., Oxford Univ. Press, New York.
- Campbell, B. A., L. M. Carter, B. R. Hawke, D. B. Campbell, and R. R. Ghent (2008), Volcanic and impact deposits of the Moon's Aristarchus plateau: A new view from Earth-based radar images, *Geology*, *36*(2), 135, doi:10.1130/g24310a.1.
- Campbell, B. A., B. R. Hawke, and D. B. Campbell (2009), Surface morphology of domes in the Marius Hills and Mons Rümker regions of the Moon from Earth-based radar data, *J. Geophys. Res.*, *114*, E01001, doi:10.1029/2008JE003253.
- Carter, J., and F. Poulet (2013), Ancient plutonic processes on Mars inferred from the detection of possible anorthositic terrains, *Nat. Geosci.*, *6*(12), 1008–1012, doi:10.1038/ngeo1995.
- Cheek, L., K. Donaldson Hanna, C. Pieters, J. Head, and J. Whitten (2013), The distribution and purity of anorthosite across the Orientale basin: New perspectives from Moon Mineralogy Mapper data, *J. Geophys. Res. Planets*, *118*, 1805–1820, doi:10.1002/jgre.20126.
- Cheek, L. C., and C. M. Pieters (2014), Reflectance spectroscopy of plagioclase-dominated mineral mixtures: Implications for characterizing lunar anorthosites remotely, *Am. Mineral.*, *99*(10), 1871–1892, doi:10.2138/am-2014-4785.
- Chevrel, S., P. Pinet, Y. Daydou, S. Lemouelic, Y. Langevin, F. Costard, and S. Erard (2009), The Aristarchus plateau on the Moon: Mineralogical and structural study from integrated Clementine UV–VIS–NIR spectral data, *Icarus*, *199*(1), 9–24, doi:10.1016/j.icarus.2008.08.005.
- Chevrel, S. D., P. C. Pinet, and J. W. Head (1999), Gruithuisen domes region: A candidate for an extended nonmare volcanism unit on the Moon, *J. Geophys. Res.*, *104*(E7), 16,515–16,529, doi:10.1029/1998JE000007.
- Cloutis, E. A., and M. J. Gaffey (1991), Pyroxene spectroscopy revisited: Spectral-compositional correlations and relationship to geothermometry, *J. Geophys. Res.*, *96*(E5), 22,809–22,826, doi:10.1029/91JE02512.
- Elbeshhausen, D., K. Wünnemann, H. Sierks, J. Vincent, and N. Oklay (2012), The effect of topography on the impact cratering process on Lutetia, *Lunar Planet. Sci.*, Abstract 1867.
- Farrand, W., G. Kramer, L. Gaddis, and G. Videen (2015), Spectral and photometric examination of pyroclastic mantles over Mons Rümker, *Lunar Planet. Sci.*, Abstract 2440.
- Gaddis, L. R., M. I. Staid, J. A. Tyburczy, B. R. Hawke, and N. E. Petro (2003), Compositional analyses of lunar pyroclastic deposits, *Icarus*, *161*(2), 262–280, doi:10.1016/s0019-1035(02)00036-2.
- Gillis, J. J., B. L. Jolliff, and R. L. Korotev (2004), Lunar surface geochemistry: Global concentrations of Th, K, and FeO as derived from lunar prospector and Clementine data, *Geochim. Cosmochim. Acta*, *68*(18), 3791–3805, doi:10.1016/j.gca.2004.03.024.
- Glotch, T. D., J. L. Bandfield, P. G. Lucey, P. O. Hayne, B. T. Greenhagen, J. A. Arnold, R. R. Ghent, and D. A. Paige (2015), Formation of lunar swirls by magnetic field standoff of the solar wind, *Nat. Commun.*, *6*, 6189, doi:10.1038/ncomms7189.
- Glotch, T. D., J. J. Hagerty, P. G. Lucey, B. R. Hawke, T. A. Giguere, J. A. Arnold, J.-P. Williams, B. L. Jolliff, and D. A. Paige (2011), The Mairan domes: Silicic volcanic constructs on the Moon, *Geophys. Res. Lett.*, *38*, L21204, doi:10.1029/2011GL049548.
- Glotch, T. D., et al. (2010), Highly silicic compositions on the Moon, *Science*, *329*(5998), 1510–1513, doi:10.1126/science.1192148.
- Greenhagen, B. T., et al. (2010), Global silicate mineralogy of the Moon from the diviner lunar radiometer, *Science*, *329*(5998), 1507–1509, doi:10.1126/science.1192196.
- Gustafson, J. O., J. F. Bell, L. Gaddis, B. Hawke, and T. A. Giguere (2012), Characterization of previously unidentified lunar pyroclastic deposits using lunar reconnaissance orbiter camera data, *J. Geophys. Res.*, *117*, E00H25, doi:10.1029/2011JE003893.
- Hagerty, J. J., D. J. Lawrence, B. R. Hawke, and L. R. Gaddis (2009), Thorium abundances on the Aristarchus plateau: Insights into the composition of the Aristarchus pyroclastic glass deposits, *J. Geophys. Res.*, *114*, E04002, doi:10.1029/2008JE003262.

- Hapke, B. (2001), Space weathering from Mercury to the asteroid belt, *J. Geophys. Res.*, *106*(E5), 10,039–10,073, doi:10.1029/2000JE001338.
- Haruyama, J., T. Matsunaga, M. Ohtake, T. Morota, C. Honda, Y. Yokota, M. Torii, Y. Ogawa, and L. W. Group (2008), Global lunar-surface mapping experiment using the lunar imager/spectrometer on SELENE, *Earth Planets Space*, *60*(4), 243–255, doi:10.1186/BF03352788.
- Haruyama, J., S. Hara, K. Hioki, A. Iwasaki, T. Morota, M. Ohtake, T. Matsunaga, H. Araki, K. Matsumoto, and Y. Ishihara (2012), Lunar global digital terrain model dataset produced from SELENE (Kaguya) terrain camera stereo observations, *Lunar Planet. Sci.*, Abstract 1200.
- Head, J. W. (1974), Lunar dark-mantle deposits—Possible clues to the distribution of early mare deposits, *Lunar Planet. Sci.*, Abstract 207–222.
- Head, J. W., and A. Gifford (1980), Lunar mare domes: Classification and modes of origin, *Moon Planets*, *22*(2), 235–258, doi:10.1007/bf00898434.
- Head, J. W., P. C. Hess, and T. B. McCord (1978), Geologic characteristics of lunar highland volcanic domes (Gruithuisen and Mairan region) and possible eruption conditions, *Lunar Planet. Sci.*, Abstract 488–490.
- Heather, D. J., S. K. Dunkin, and L. Wilson (2003), Volcanism on the Marius Hills plateau: Observational analyses using Clementine multispectral data, *J. Geophys. Res.*, *108*(E3), 5017, doi:10.1029/2002JE001938.
- Heiken, G. H., D. S. McKay, and R. Brown (1974), Lunar deposits of possible pyroclastic origin, *Geochim. Cosmochim. Acta*, *38*(11), 1703–1704, 1705–1718, doi:10.1016/0016-7037(74)90187-2.
- Hiesinger, H., J. W. Head, U. Wolf, R. Jaumann, and G. Neukum (2003), Ages and stratigraphy of mare basalts in Oceanus Procellarum, Mare Nubium, Mare Cognitum, and Mare Insularum, *J. Geophys. Res.*, *108*(E7), 5065, doi:10.1029/2002JE001985.
- Horgan, B. H. N., E. A. Cloutis, P. Mann, and J. F. Bell (2014), Near-infrared spectra of ferrous mineral mixtures and methods for their identification in planetary surface spectra, *Icarus*, *234*, 132–154, doi:10.1016/j.icarus.2014.02.031.
- Huang, J., L. Xiao, X. He, L. Qiao, J. Zhao, and H. Li (2011), Geological characteristics and model ages of Marius Hills on the Moon, *J. Earth Sci.*, *22*(5), 601–609, doi:10.1007/s12583-011-0211-8.
- Huang, Q., Z. Xiao, and L. Xiao (2014), Subsurface structures of large volcanic complexes on the nearside of the Moon: A view from GRAIL gravity, *Icarus*, *243*, 48–57, doi:10.1016/j.icarus.2014.09.009.
- Hurwitz, D. M., J. W. Head, L. Wilson, and H. Hiesinger (2012), Origin of lunar sinuous rilles: Modeling effects of gravity, surface slope, and lava composition on erosion rates during the formation of Rima Prinz, *J. Geophys. Res.*, *117*, E00H14, doi:10.1029/2011JE004000.
- Ip, W.-H., J. Yan, C.-L. Li, and Z.-Y. Ouyang (2014), Preface: The Chang'e-3 lander and rover mission to the Moon, *Res. Astron. Astrophys.*, *14* (12), 1511, doi:10.1088/1674-4527/14/12/001.
- Isaacson, P. J., N. E. Petro, C. M. Pieters, S. Besse, J. W. Boardman, R. N. Clark, R. O. Green, S. Lundeen, E. Malaret, and S. McLaughlin (2013), Development, importance, and effect of a ground truth correction for the Moon Mineralogy Mapper reflectance data set, *J. Geophys. Res. Atmos.*, *118*, 369–381, doi:10.1002/jgre.20048.
- Ivanov, M. A., J. W. Head, and A. Bystrov (2016), The lunar Gruithuisen silicic extrusive domes: Topographic configuration, morphology, ages, and internal structure, *Icarus*, *273*, 262–283, doi:10.1016/j.icarus.2015.12.015.
- Jawin, E. R., S. Besse, L. R. Gaddis, J. M. Sunshine, J. W. Head, and S. Mazrouei (2015), Examining spectral variations in localized lunar dark mantle deposits, *J. Geophys. Res. Planets*, *120*, 1310–1331, doi:10.1002/2014JE004759.
- Jolliff, B. L., J. J. Gillis, L. A. Haskin, R. L. Korotev, and M. A. Wieczorek (2000), Major lunar crustal terranes: Surface expressions and crust-mantle origins, *J. Geophys. Res.*, *105*(E2), 4197–4216, doi:10.1029/1999JE001103.
- Jolliff, B. L., S. A. Wiseman, S. J. Lawrence, T. N. Tran, M. S. Robinson, H. Sato, B. R. Hawke, F. Scholten, J. Oberst, and H. Hiesinger (2011), Non-mare silicic volcanism on the lunar farside at Compton-Belkovich, *Nat. Geosci.*, *4*(8), 566–571, doi:10.1038/ngeo1212.
- Jozwiak, L. M., J. W. Head, M. T. Zuber, D. E. Smith, and G. A. Neumann (2012), Lunar floor-fractured craters: Classification, distribution, origin and implications for magmatism and shallow crustal structure, *J. Geophys. Res.*, *117*, E11005, doi:10.1029/2012JE004134.
- Kaur, P., S. Bhattacharya, P. Chauhan, Ajai, and A. S. Kiran Kumar (2013), Mineralogy of Mare Serenitatis on the near side of the Moon based on Chandrayaan-1 Moon Mineralogy Mapper (M3) observations, *Icarus*, *222*(1), 137–148, doi:10.1016/j.icarus.2012.10.020.
- Kodama, S., et al. (2010), Characterization of Multiband Imager aboard SELENE, *Space Sci. Rev.*, *154*(1–4), 79–102, doi:10.1007/s11214-010-9661-z.
- Kusuma, K. N., N. Sebastian, and S. V. S. Murty (2012), Geochemical and mineralogical analysis of Gruithuisen region on Moon using M3 and DIVINER images, *Planet. Space Sci.*, *67*(1), 46–56, doi:10.1016/j.pss.2012.02.012.
- Lawrence, D., W. Feldman, R. Elphic, R. Little, T. Prettyman, S. Maurice, P. Lucey, and A. Binder (2002), Iron abundances on the lunar surface as measured by the lunar prospector gamma-ray and neutron spectrometers, *J. Geophys. Res.*, *107*(E12), 13-11–13-26, doi:10.1029/2001JE001530.
- Lawrence, S. J., et al. (2013), LRO observations of morphology and surface roughness of volcanic cones and lobate lava flows in the Marius Hills, *J. Geophys. Res. Planets*, *118*, 615–634, doi:10.1002/jgre.20060.
- Le Mouélic, S., Y. Langevin, S. Erard, P. Pinet, S. Chevrel, and Y. Daydou (2000), Discrimination between maturity and composition of lunar soils from integrated Clementine UV-visible/near-infrared data: Application to the Aristarchus plateau, *J. Geophys. Res.*, *105*(E4), 9445, doi:10.1029/1999JE001196.
- Lena, R., C. Wöhler, J. Phillips, M. Wirths, and M. T. Bregante (2007), Lunar domes in the Doppelmayer region: Spectrophotometry, morphometry, rheology, and eruption conditions, *Planet. Space Sci.*, *55*(10), 1201–1217, doi:10.1016/j.pss.2007.01.007.
- Lena, R., C. Wöhler, M. T. Bregante, P. Lazzarotti, and S. Lammel (2008), Lunar domes in Mare Undarum: Spectral and morphometric properties, eruption conditions, and mode of emplacement, *Planet. Space Sci.*, *56*(3–4), 553–569, doi:10.1016/j.pss.2007.11.010.
- Logan, L. M., G. R. Hunt, J. W. Salisbury, and S. R. Balsamo (1973), Compositional implications of Christiansen frequency maximums for infrared remote sensing applications, *J. Geophys. Res.*, *78*(23), 4983–5003, doi:10.1029/JB078i023p04983.
- Lucey, P., D. Paige, B. Greenhagen, J. Bandfield, and T. Glotch (2010), Comparison of Diviner Christiansen Feature position and visible albedo: Composition and space weathering implications, *Lunar Planet. Sci.*, Abstract 1600.
- Lucey, P. G., B. T. Greenhagen, E. Song, J. A. Arnold, M. Lemelin, K. D. Hanna, N. E. Bowles, T. D. Glotch, and D. A. Paige (2017), Space weathering effects in diviner lunar radiometer multispectral infrared measurements of the lunar Christiansen Feature: Characteristics and mitigation, *Icarus*, *283*, 343–351, doi:10.1016/j.icarus.2016.05.010.
- McEwen, A. S., M. S. Robinson, E. M. Eliason, and P. G. Lucey (1994), Clementine observations of the Aristarchus region of the Moon, *Science*, *266*(5192), 1858, doi:10.1126/science.266.5192.1858.
- Michael, G. G., and G. Neukum (2010), Planetary surface dating from crater size–frequency distribution measurements: Partial resurfacing events and statistical age uncertainty, *Earth Planet. Sci. Lett.*, *294*(3–4), 223–229, doi:10.1016/j.epsl.2009.12.041.
- Mustard, J. F., et al. (2011), Compositional diversity and geologic insights of the Aristarchus crater from Moon Mineralogy Mapper data, *J. Geophys. Res.*, *116*, E00G12, doi:10.1029/2010JE003726.
- Neal, C. R., and L. A. Taylor (1992), Petrogenesis of mare basalts: A record of lunar volcanism, *Geochim. Cosmochim. Acta*, *56*(6), 2177–2211, doi:10.1016/0016-7037(92)90184-K.

- Neukum, G., B. A. Ivanov, and W. K. Hartmann (2001), Cratering Records in the Inner Solar System in relation to the lunar reference system, *Space Sci. Rev.*, *96*, 55–86.
- Noble, S. K., C. M. Pieters, and L. P. Keller (2007), An experimental approach to understanding the optical effects of space weathering, *Icarus*, *192*(2), 629–642, doi:10.1016/j.icarus.2007.07.021.
- Ohtake, M., et al. (2009), The global distribution of pure anorthosite on the Moon, *Nature*, *461*(7261), 236–240, doi:10.1038/nature08317.
- Otake, H., M. Ohtake, and N. Hirata (2012), Lunar iron and titanium abundance algorithms based on SELENE (Kaguya) Multiband Imager data, *Lunar Planet. Sci.*, Abstract 1905.
- Paige, D., M. Foote, B. Greenhagen, J. Schofield, S. Calcutt, A. Vasavada, D. Preston, F. Taylor, C. Allen, and K. Snook (2010), The lunar reconnaissance orbiter diviner lunar radiometer experiment, *Space Sci. Rev.*, *150*(1–4), 125–160, doi:10.1007/s11214-009-9529-2.
- Pieters, C. M., M. I. Staid, E. M. Fischer, S. Tompkins, and G. He (1994), A sharper view of impact craters from clementine data, *Science*, *266*(5192), 1844–1848, doi:10.1126/science.266.5192.1844.
- Pieters, C. M., L. A. Taylor, S. K. Noble, L. P. Keller, B. Hapke, R. V. Morris, C. C. Allen, D. S. McKay, and S. Wentworth (2000), Space weathering on airless bodies: Resolving a mystery with lunar samples, *Meteorit. Planet. Sci.*, *35*(5), 1101–1107, doi:10.1111/j.1945-5100.2000.tb01496.x.
- Pieters, C. M., J. Boardman, B. Buratti, A. Chatterjee, R. Clark, T. Glavich, R. Green, J. Head, P. Isaacson, and E. Malaret (2009), The Moon Mineralogy Mapper (M<sup>3</sup>) on Chandrayaan-1, *Curr. Sci.*, *96*(4), 500–505.
- Pieters, C. M., et al. (2011), Mg-spinel lithology: A new rock type on the lunar farside, *J. Geophys. Res.*, *116*, E00G08, doi:10.1029/2010JE003727.
- Basaltic Volcanism Study Project (1981), *Basaltic Volcanism on the Terrestrial Planets*, pp. 702–887, Lunar and Planetary Institute, New York.
- Qiao, L., L. Xiao, J. Zhao, Q. Huang, and J. Haruyama (2014), Geological features and evolution history of Sinus Iridum, the Moon, *Planet. Space Sci.*, *101*(2014), 37–52, doi:10.1016/j.pss.2014.06.007.
- Robinson, M. S., et al. (2010), Lunar Reconnaissance Orbiter Camera (LROC) instrument overview, *Space Sci. Rev.*, *150*(1–4), 81–124, doi:10.1007/s11214-010-9634-2.
- Salisbury, J. W., and L. S. Walter (1989), Thermal infrared (2.5–13.5  $\mu\text{m}$ ) spectroscopic remote sensing of igneous rock types on particulate planetary surfaces, *J. Geophys. Res.*, *94*(B7), 9192–9202, doi:10.1029/JB094iB07p09192.
- Schmincke, H.-U. (2004), *Volcanism*, pp. 24–27, Springer Science & Business Media, Berlin.
- Scott, D. H., and R. E. Eggleton (1973), Geologic map of the Rümker quadrangle of the Moon, *US Geol. Invest. Ser. I-805*, U.S. Geol. Surv., Boulder, Colo.
- Smith, E. I. (1974), Rümker Hills: A lunar volcanic dome complex, *Moon*, *10*(2), 175–181, doi:10.1007/BF00655718.
- Spudis, P. D., P. J. McGovern, and W. S. Kiefer (2013), Large shield volcanoes on the Moon, *J. Geophys. Res. Planets*, *118*, 1063–1081, doi:10.1002/jgre.20059.
- Stöfler, D., and G. Ryder (2001), Stratigraphy and isotope Ages of lunar geologic units: Chronological standard for the inner solar system, *Space Sci. Rev.*, *96*, 954, doi:10.1007/978-94-017-1035-0\_2.
- Sun, Z., T. Zhang, H. Zhang, Y. Jia, H. Zhang, J. Chen, X. Wu, and Z. Shen (2014), The technical design and achievements of Chang'E-3 probe, *Sci. Sinica Tech.*, *44*(4), 331–343, doi:10.1360/092014-3.
- Sunshine, J. M., and C. M. Pieters (1998), Determining the composition of olivine from reflectance spectroscopy, *J. Geophys. Res.*, *103*(E6), 13675–13688, doi:10.1029/98JE01217.
- Sunshine, J. M., C. M. Pieters, and S. F. Pratt (1990), Deconvolution of mineral absorption bands: An improved approach, *J. Geophys. Res.*, *95*(B5), 6955–6966, doi:10.1029/JB095iB05p06955.
- Wöhler, C., and R. Lena (2009), Lunar intrusive domes: Morphometric analysis and laccolith modelling, *Icarus*, *204*(2), 381–398, doi:10.1016/j.icarus.2009.07.031.
- Wöhler, C., R. Lena, P. Lazzarotti, J. Phillips, M. Wirths, and Z. Pujic (2006), A combined spectrophotometric and morphometric study of the lunar mare dome fields near Cauchy, Arago, Hortensius, and Milichius, *Icarus*, *183*(2), 237–264, doi:10.1016/j.icarus.2006.03.003.
- Wöhler, C., R. Lena, and K. C. Pau (2007a), The lunar dome complex Mons Rümker: Morphometry, rheology, and mode of emplacement, *Lunar Planet. Sci.*, Abstract 1091.
- Wöhler, C., R. Lena, and J. Phillips (2007b), Formation of lunar mare domes along crustal fractures: Rheologic conditions, dimensions of feeder dikes, and the role of magma evolution, *Icarus*, *189*(2), 279–307, doi:10.1016/j.icarus.2007.01.011.
- Wöhler, C., R. Lena, and K. C. Pau (2010), Lunar intrusive domes on the floor of grimaldi and near Aristillus, *Lunar Planet. Sci.*, Abstract 1478.
- Wagner, R., J. W. Head, U. Wolf, and G. Neukum (2002), Stratigraphic sequence and ages of volcanic units in the Gruithuisen region of the Moon, *J. Geophys. Res.*, *107*(E11), 14-11–14-15, doi:10.1029/2002JE001844.
- Wagner, R., J. W. Head, U. Wolf, and G. Neukum (2010), Lunar red spots: Stratigraphic sequence and ages of domes and plains in the Hansteen and helmet regions on the lunar nearside, *J. Geophys. Res.*, *115*, E06015, doi:10.1029/2009JE003359.
- Watters, T. R., M. S. Robinson, R. A. Beyer, M. E. Banks, J. F. Bell, M. E. Pritchard, H. Hiesinger, C. H. van der Bogert, P. C. Thomas, and E. P. Turtle (2010), Evidence of recent thrust faulting on the Moon revealed by the lunar reconnaissance orbiter camera, *Science*, *329*(5994), 936–940, doi:10.1126/science.1189590.
- Weitz, C. M., and J. W. Head (1999), Spectral properties of the Marius Hills volcanic complex and implications for the formation of lunar domes and cones, *J. Geophys. Res.*, *104*(E8), 18,933, doi:10.1029/1998JE000630.
- Wilson, L., and I. I. J. W. Head (2003), Lunar Gruithuisen and Mairan domes: Rheology and mode of emplacement, *J. Geophys. Res.*, *108*(E2), 5012, doi:10.1029/2002JE001909.
- Wood, C. (1984), Calderas: A planetary perspective, *J. Geophys. Res.*, *89*(B10), 8391–8406, doi:10.1029/JB089iB10p08391.
- Wray, J. J., S. T. Hansen, J. Dufek, G. A. Swayze, S. L. Murchie, F. P. Seelos, J. R. Skok, R. P. Irwin, and M. S. Ghiorso (2013), Prolonged magmatic activity on Mars inferred from the detection of felsic rocks, *Nat. Geosci.*, *6*(12), 1013–1017, doi:10.1038/ngeo1994.
- Wyrick, D., D. A. Ferrill, A. P. Morris, S. L. Colton, and D. W. Sims (2004), Distribution, morphology, and origins of Martian pit crater chains, *J. Geophys. Res.*, *109*, E06005, doi:10.1029/2004JE002240.
- Xiao, L., et al. (2015), A young multilayered terrane of the northern Mare Imbrium revealed by Chang'E-3 mission, *Science*, *347*(6227), 1226–1229, doi:10.1126/science.1259866.
- Zhang, F., Y. L. Zou, Y. C. Zheng, X. H. Fu, and Y. C. Zhu (2014), Lunar mare basalts in the Aristarchus region: Implications for the stratigraphic sequence from Clementine UVVIS data, *Icarus*, *227*, 132–151, doi:10.1016/j.icarus.2013.09.011.
- Zhao, J., J. Huang, L. Qiao, Q. Huang, J. Wang, Q. He, and L. Xiao (2014), Geologic characteristics of the Chang'E-3 exploration region, *Sci. China-Phys. Mech. Astron.*, *57*(3), 569–576, doi:10.1007/s11433-014-5399-z.
- Zou, Y., and W. Li (2017), Scientific visions of lunar research-station from China, *Lunar Planet. Sci.*, Abstract 1730.